APPLICATION OF DEFORMABLE MODELS FOR THE DETECTION OF ACUTE RENAL REJECTION

Ayman El-Baz, Aly A. Farag, and Seniha E. Yuksel

Computer Vision & Image Processing Laboratory (CVIP)
University of Louisville, Louisville, Kentucky

Mohamed E.A. El-Ghar, Tarek A. Eldiasty,
and Mohamed A. Ghoneim

Urology and Nephrology Department
University of Mansoura, Mansoura, Egypt

Acute rejection is the most common reason for graft failure after kidney transplantation, and early detection is crucial to survival of function in the transplanted kidney. In this study we introduce a new framework for automatic classification of normal and acute rejection transplants from Dynamic Contrast Enhanced Magnetic Resonance Images (DCE-MRI). The proposed framework consists of three main steps. The first isolates the kidney from the surrounding anatomical structures by evolving a deformable model based on two density functions; the first function describes the distribution of the gray level inside and outside the kidney region and the second describes the prior shape of the kidney. In the second step, nonrigid registration algorithms are employed to account for the motion of the kidney due to the patient's breathing. In the third step, the perfusion curves that show transportation of the contrast agent into the tissue are obtained from the segmented cortex of the whole image sequence of the patient. In the final step, we collect four features from these curves and use Bayesian classifiers to distinguish between acute rejection and normal transplants. Applications of the proposed approach yield promising results that would, in the near future, replace the use of current technologies such as nuclear imaging and ultrasonography, which are not specific enough to determine the type of kidney dysfunction.

Address all correspondence to: Dr. Aly A. Farag, Professor of Electrical and Computer Engineering, University of Louisville, CVIP Lab, Room 412, Lutz Hall, 2301 South 3rd Street, Louisville, KY 40208, USA. Phone: (502) 852-7510, Fax: (502) 852-1580. aafara01@louisville.edu.

1. INTRODUCTION

In the United States, more than 12000 renal transplantations are performed each year [1], but the transplanted kidneys face a number of surgical and medical complications that cause a decrease in their functionality. Although such a decrease in functionality can be reversed by proper treatment strategies and drug therapies [2], the currently used techniques are not specific enough to diagnose the possible diseases. For example, *measurement of creatinine levels* can be affected by diet and medications [3]. *Clearances of inulin and DTPA* require multiple blood and urine tests, and they provide information on both kidneys together, but not unilateral information [4]. On the other hand, imaging tests are favorable since they provide information on each kidney separately. However, the most frequently used imaging technique, *scintigraphy* (also called nuclear imaging), preferred for its good functional information, does not provide good spatial resolution. Without good spatial resolution, precise anatomical detail cannot be obtained, so the diseases that affect the different parts of the kidney (such as the cortex and medulla) cannot be diagnosed accurately [5]. Moreover, scintigraphy exposes the patients to a small dose of radioactivity [6]. Another traditional imaging modality, *Computed Tomography* (CT), uses nephrotoxic contrast agents and exposes patients to radiation despite its superior functional and anatomical information [7]. *Ultrasonography* has been found to show normal findings despite severe renal dysfunction [8], and several studies on color Doppler sonography and power Doppler sonography (e.g., [9–11]) have not been able to yield significant information to evaluate renal function. Therefore, despite all its high costs and morbidity rates, *biopsy* is remains the gold standard for diagnosis after renal transplantation. Unfortunately, the downside of biopsy is that patients are subjected to such risks as bleeding and infection; moreover, the relatively small needle biopsies may lead to over- or underestimation of the extent of inflammation in the entire graft [12]. Hence, a noninvasive and repeatable technique would not only be useful but is needed to ensure survival of transplanted kidneys. For this reason, a fairly new imaging technique, Dynamic Contrast Enhanced Resonance Imaging (DCE-MRI), has gained considerable attention due to its ability to yield superior anatomical and functional information. With DCE-MRI it has been possible to distinguish the different structures of the kidney (such as the cortex and medulla) in a noninvasive way, and, combined with function information, image analysis with DCE-MRI can help in detecting diseases that affect the different parts of renal transplants. Therefore, the CVIP Lab at the University of Louisville and the Urology and Nephrology Center at the University of Mansoura have begun an ongoing collaboration to detect acute rejection from normal functioning of transplants. This study focuses on the DCE-MRI findings of this collaboration.

Acute rejection is the attack of the recipient's immune system on a foreign kidney. Therefore, prompt anti-rejection therapy can suppress the immune system and save the transplanted kidney [13]. Moreover, acute rejection is the most important cause of renal dysfunction [14] among the diagnostic possibilities following renal transplantation (e.g., acute rejection, acute tubular necrosis, cyclosporin toxicity, and obstruction [15]). Therefore, early and noninvasive detection of acute rejection is crucial.

Within the framework of our collaborative research, patients' urine and blood are tested daily at 9:00 a.m. for detection of acute rejection after transplantation. Following these tests, the abdomen is imaged using Color Doppler Ultrasonography during the first 2 weeks. If circumstances do not require it previously, DCE-MRI is performed at the end of the 2-week nursing period. If in addition to the other tests, DCE-MRI findings are normal, then no further action is taken. However, if the findings are abnormal, a biopsy is performed to determine the type of rejection or the type of kidney disease. Images of patients with histopathological diagnosis of acute rejection episodes and normal transplant images are sent to the University of Louisville to test and train the analysis software. In this study, we focused on Dynamic Contrast Enhanced Resonance Imaging (DCE-MRI) findings.

In Dynamic Contrast Enhanced Resonance Imaging (DCE-MRI), the contrast agent gadolinium diethylene triamine pentaacetic acid (Gd-DTPA) is injected into the bloodstream. During its passage from the blood to the kidneys and on to the urinary system, the kidneys are imaged rapidly and repeatedly. As the Gd-DTPA perfuses into the kidney, it causes a change in tissue relaxation time, which creates a contrast change (intensity increase/decrease) in the images. If the intensity is averaged over the kidney tissue (either cortex or medulla) and plotted against time, a signal curve (change in average intensity vs. time) is obtained. Such intensity curves obtained from the kidney are called MR renograms [5]. The pattern of an MR renogram is an indicator of the kidney's degree of functionality, and it can be used in determining the type of the rejection or dysfunction. Moreover, since DCE-MRI provides good anatomical information, separate renograms can be obtained for the cortical and medullary structures of the kidney, which will help in distinguishing the diseases that affect different parts of the kidney. Hence, a typical protocol using dynamic MRI involves the following steps: (1) collecting a sequence of images from the kidney region as the contrast agent perfuses through the kidney; (2) following the contrast difference in the kidney over time (image intensity information from the cortex varies with time as the contrast agent perfuses through the kidney); and (3) establishing a correspondence between change of contrast in the image sequence and kidney status. Such a protocol requires some intermediate image processing steps — namely, segmentation, registration, and classification — explained in later sections of this chapter.

2. RELATED WORK IN RENAL IMAGE ANALYSIS USING DCE-MRI

Starting with examination of rats, studies to acquire functional, dynamic, and anatomic information on the kidneys date back to the early 1980s, covering a variety of objectives from simply understanding the normal behavior of a kidney to detecting kidney diseases. The potential of DCE-MRI to help understand kidney function has been investigated in various studies (see [7, 16–28], to cite a few). This imaging modality has been applied to various kidney diseases in several other studies, such as for detection of renal ischemic lesions [29], for evaluation of renal failure [30], for acute tubular necrosis [31], for assessment of chronic medical nephropathies [32], to differentiate obstructive from nonobstructive hydronephrosis [33, 34], to evaluate rejection [35], to differentiate acute tubular necrosis from transplant rejection in patients with delayed kidney function [36], to differentiate acute tubular necrosis from acute transplant rejection [14], for functional and morphological evaluation of live kidney donors [37], to study renal function in nephrolithiasis and hydronephrosis [26], to observe the effect of hypertension on kidney function [38], and for evaluation of normal and transplanted rat kidneys [12].

These studies are significant, as they have ascertained DCE-MRI to be a very promising technique not only for assessing renal blood flow and consequently help understand kidney function, but also to evaluate several clinical disorders. However, most of these studies were performed by radiologists who selected a region of interest (ROI) (a small window) from the kidney and followed signal change within this region of interest. Unfortunately, such approaches not only require manual interaction of the operators, but also ROI selection biases the final decision and brings up the same issue of over- or underestimating the problem in the entire graft, just as with biopsy. Moreover, manual window selection, and generating a function curve from this window over a time-sequence of images, assumes that the kidneys (renal contours) remain exactly the same from scan to scan. However, renal contours may not always exactly match due to patient movement or breathing effects; therefore, image registration schemes should be applied first before ROI selection. Also, to automate the algorithm and to cancel ROI dependency, segmentation algorithms that can separate the kidney from the surrounding structures, and that can further separate the kidney into its cortex and medulla compartments are needed. In the remainder of this section, we discuss the previous computerized studies that made use of image processing techniques.

To the best of our knowledge, the first computerized renal image analysis scheme was developed by Gerig et al. [25] in 1992. In this study, the prior contour information for each study was obtained by manually drawing the contour from one image. For the rest of the images, image discontinuities (edges) were detected, and the model curve was matched to these edges using a Hough transform. To extend the algorithm to arbitrary rotation and translation, the model contour was

rotated and translated to get the best correlation, giving the registration parameters of the image. The rotation in this scheme was limited to ∓ 4 degrees in 1-degree steps. For the cases of when the patient inadvertently moved or breathed, detection of kidney contour was severely impeded; therefore, a 50% vote rule was defined, that is, at least 50% of the kidney needed to be detected for registration to work. A similar procedure with some extensions was used by Yim et al. in [22].

The handicaps of this image analysis scheme can be listed as follows: (i) the need for manual selection of a contour for each study; (ii) the problems that can be faced in case of a large movement by the patient, and (iii) the great computational expense of the Hough transform (the algorithm was implemented in parallel in [25], and one patient took about an hour to evaluate). Moreover, this registration method is highly dependent on the edge detection filter. Although the strength of edge detection was increased by using opposed-phase gradient echo imaging that puts a dark line between the water-based kidney and the perirenal fatty tissue, still, the algorithm worked better in smaller areas since increasing the field of view (FOV) parameter caused the algorithm to match more partial contours. Following this same procedure, healthy volunteers and hydronephrosis patients were compared in [26], and DCE-MRI was shown to be a reliable method for kidney analysis.

Noting the lack of special protocols and the consequent problems with edge detection in the registration process, the second image analysis study came from Giele et al. [28] in 2001, where three movement correction methods were compared based on image matching, phase difference movement detection (PDMD), and cross-correlation. In all these methods, a mask is generated from the best image manually, and its similarity to a given image is calculated. Consequently, the (i, j) values that give the highest similarity become the translation parameters for the given image. Among these methods, the PDMD method demonstrated the best performance, but only with an 68% accuracy compared to the results of a radiologist. More importantly, in all three registration algorithms only translational motion was handled and rotational motion was not mentioned, the existence of which has been discussed in a number of studies (see [26, 39, 40]).

For segmentation of the kidneys, Priester et al. [41] subtracted the average of pre-contrast images from the average of early-enhancement images, and thresholded the subtraction image to obtain a black-and-white mask kidney image. Following this step, objects smaller than a certain size were removed and the remaining kidney object was closed with erosion operations and manual interactions to obtain a kidney contour.

This approach was furthered by Giele et al. [5] by applying an erosion filter to the mask image to obtain a contour via a second subtraction stage. The possible gaps in this contour were closed by a hull function to get the boundary of the kidney, then via repeated erosions applied to this contour, several rings were obtained, which formed the basics of the segmentation of the cortex from the medulla structures. Of course, in such a segmentation the medulla structures were intermixed

with the cortex structures, so a correlation study had to be applied to better classify the cortical and medullary pixels.

Also in 2001, Boykov et al. [42] presented the use of graph cuts using Markov models. In this algorithm, each voxel is described as a vector of intensity values over time, and initially, several seed points are put on the objects and on the background to give user-defined constraints as well as an expert sample of intensity curves. These expert samples of intensity curves are used to compute a two-dimensional histogram that would be used further as a data penalty function in minimizing the energy function in the Markov model. Although the results looked promising, this algorithm was tested only on one kidney volume, and manual interaction was still required.

Following these studies, computerized image analysis schemes for the registration and segmentation of kidneys were introduced by Sun et al. [12, 21, 23, 24, 40, 43] in a series of studies performed on rats and human subjects. The study on humans ([21, 40]) made use of a multistep registration approach. Initially, the edges were aligned using an image gradient-based similarity measure considering only translational motion. Once roughly aligned, a high-contrast image was subtracted from a pre-contrast image to obtain a kidney contour, which was then propagated over the other frames searching for the rigid registration parameters (rotation and translation). For segmentation of the cortex and medulla, the level sets approach of Chan et al. [44] was used.

In most of these previous efforts, healthy transplants were used in the image analysis, so the edge detection algorithms were applicable. However, in the case of acute rejection patients, the uptake of contrast agent was decreased, so edge detection algorithms generally failed in giving connected contours. Therefore, in our approach, we avoid edge detection schemes; instead, we combine the use of gray-level and prior shape information.

3. RELATED WORK IN SHAPE-BASED SEGMENTATION

Both active contours and level sets tend to fail in the case of noise, poor image resolution, diffused boundaries, or occluded shapes if they do not take advantage of the a priori models. Four of the popular segmentation algorithms that make use of only gray-level information are shown in Figure 1 implemented with ITK Version 2.0; namely, thresholding level sets [45], fast marching level sets [46], and geodesic active contours [47]. However, especially in the area of medical imaging, organs have well-constrained forms within a family of shapes [48]. Thus, additional constraints based on the shape of the objects have been greatly needed aside from the gray-level information of these objects.

Therefore, to allow shape-driven segmentation, Leventon et al. [49] used a shape prior whose variance was obtained thorough Principal Component Analysis (PCA), and used this shape prior to evolving the level sets to the maximum a
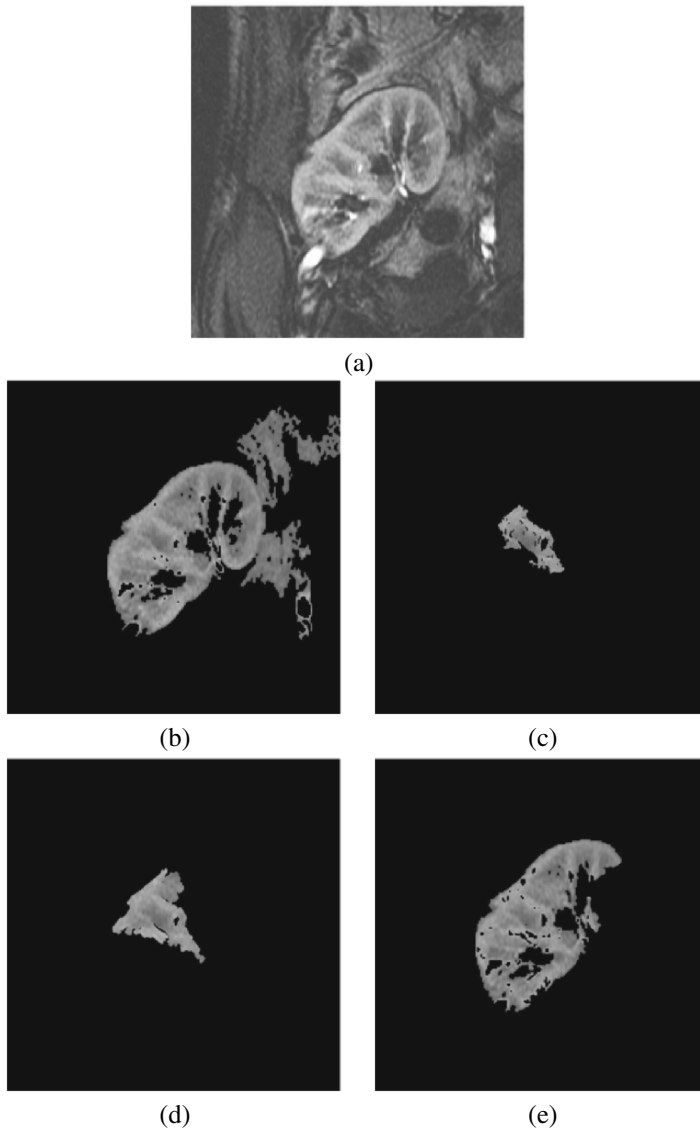
Figure 1. (a) Kidney to be segmented from the surrounding organs. The results of some popular segmentation algorithms that depend only on gray-level and gradient information, (b) connected thresholding, (c) fast marching level sets, (d) geodesic active contours, and (e) thresholding level sets segmentation.

posteriori shape. Chen et al. [50] calculated an average of a registered training set to be a shape prior, and defined an energy functional that basically minimizes a Euclidean distance between a given point and its shape prior. In [51] a representation of the segmenting curve was generated based on the pose and shape parameters of a training set, which were optimized using a region-based energy functional. In [48, 52] a shape prior and its variance obtained from training data were used to define a Gaussian distribution, which was then used in the external energy component of a level sets framework. In Litvin et al.'s study [53], a shape boundary prior was formed from the features of the boundary, and this boundary was used within a level set framework.

Recently, Tsai et al. [54] used a deterministic model to represent the desired shape as a linear combination of weighted signed 2D distance maps and estimated these weights by minimizing a mutual information-based cost function. In addition, Yang et al. [55] described the shapes with a multidimensional Gaussian probability model of these weights.

Different from previous studies, in our segmentation approach the contour points move by comparing the energy at the neighboring points; but with different energy terms that will be explained in Section 5. With this new energy component, the contour moves with both the current gray-level and prior shape information; thus, it does not get stuck in edge points, and handles intricate shapes. Also different from previous studies, the prior shape information is a density estimation of the signed distance map inside and outside the object of interest, not the average image itself. This algorithm overcomes the inability of deformable models to stop in a state of high noise or in the case of missing edges.

During the remainder of the present study, we will discuss the data acquisition protocol in Section 4 and give an overview of the components of the framework. In Section 5 we will introduce our segmentation approach, starting with the general idea of the method. We will then go into the details and explain shape model construction from a database in Section 5.1. In Section 5.2 we will offer an introduction to our density estimation scheme; in Sections 5.3, 5.4, and 5.5 we will explain the details of implementation of our density estimation framework. Section 5.3 introduces a modified EM algorithm, and Section 5.4 introduces a sequential EM algorithm to closely initialize the parameters of the EM estimation. Section 5.5 explains classification of the Gaussian components and the stopping conditions. Given the shape model and the density estimations for the shape model and the gray level of an image to segment, in Section 5.6 we explain how the deformable model evolves in an image. After the whole sequence of a patient is segmented, we introduce a nonrigid registration algorithm in Section 6 that deforms the kidney object on isocontours. Once all the images are aligned, the cortex of one early-enhancement image is extracted in Section 7, and then used as a mask to calculate the average cortex intensity signal in the rest of the sequence. The results of classification based on these signals are presented in Section 8, and

the study is concluded in Section 9 with speculation about future work and further discussion.

4.   METHODS AND DATA ACQUISITION

During development of this study, we observed that good selection of a DCE-MRI imaging protocol is as important as the image analysis — if not more important. The key point in the protocol is to take the images as quickly as possible while trying to conserve the quality. A compromise on image quality results in too much noise and partial volume effects; on the other hand, a compromise on speed results in fewer data points, which prevents us from being able to classify signals. Therefore, with collaborative efforts, the protocol was modified a number of times to acquire standard and better-quality imaging. The protocol described below has been found to be optimal with the current MRI hardware (Signa Horizon GE 1.5T scanner).

In our protocol, gradient-echo T1 imaging is employed by a Signa Horizon GE 1.5T scanner (Signa Horizon LX Echo speed; General Electric Medical Systems, Milwaukee, WI, USA) with the use of a phased-array Torso surface coil; the contrast agent (Gadolinium DTPA) is introduced via a wide-bore veno-catheter, placed at the antecubital vein, at a rate of 3–4 ml/sec, with a dose of 0.2 ml/kg·BW. Images are taken at 5 mm thickness with no interslice gap, the repetition time (TR) is 34 msec, the TE minimum, the field of view (FOV) is 42×42 cm, and with a 600×600 matrix. For each patient, 150 temporal sequences of coronal scans are taken at 4-second intervals. A sample of what a DCE-MRI looks like with this protocol is shown in Figure 2.

With this protocol, we propose the following framework [56] for image analysis, as shown in Figure 3:

1. Segmentation of the kidneys from the abdomen images.

2. Nonrigid registration for motion compensation.

3. Renogram generation.

4. Feature extraction.

5. Classification of acute rejection patients and normal transplants.

5.   KIDNEY SEGMENTATION

Accurate segmentation of the kidney from DCE-MRI is a challenge, since the gray-level distribution of the kidney and surrounding organs is not highly distinguishable; we thus add additional constraints based on the shape of the objects
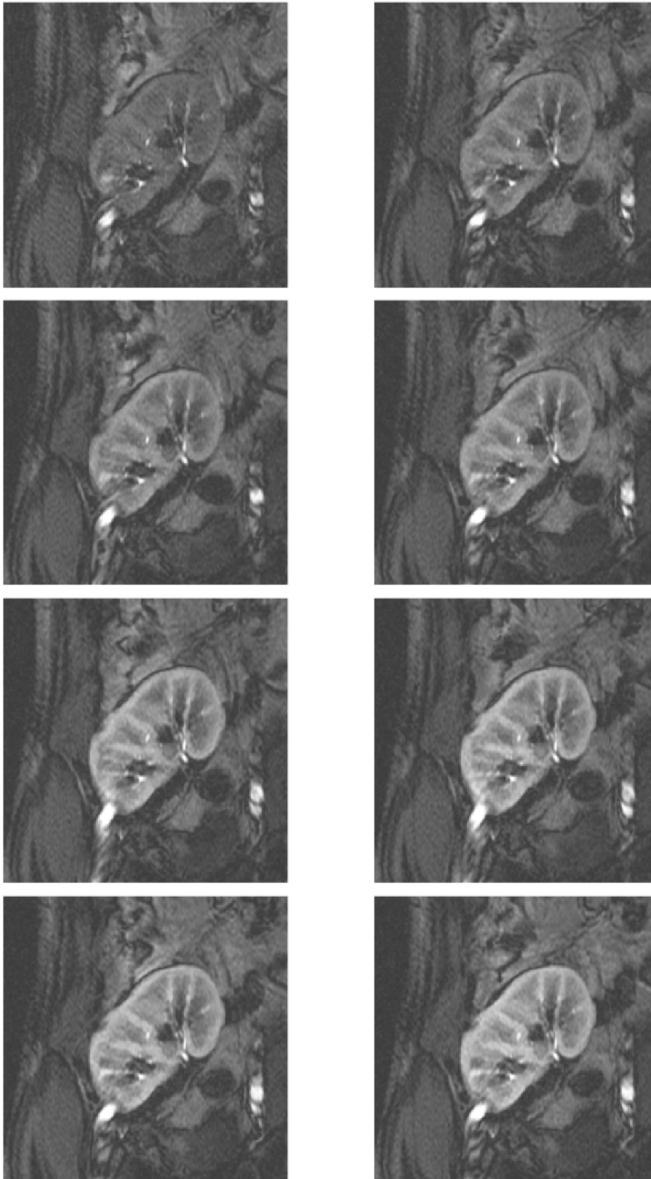
Figure 2. Example of a DCE-MRI series. For each patient, 150 images are taken from one cross-section with 4-second intervals. Eight of one subject (numbers 1, 4, 5, 6, 10, 15, 21, 27) are shown here to give an idea of the protocol.
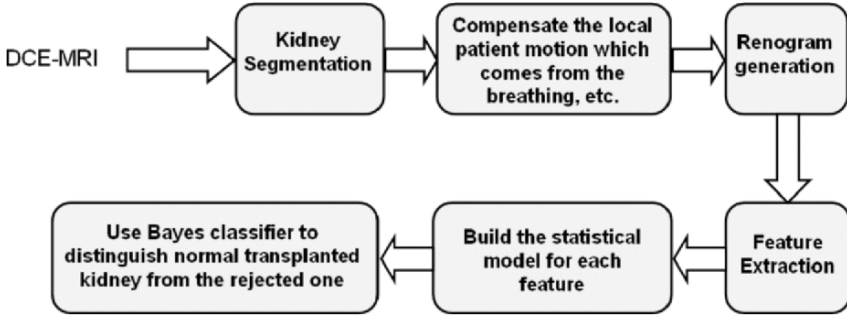
Figure 3. Block diagram of the proposed image analysis to create a CAD system for renal transplantation. See attached CD for color version.

to control evolution of the deformable models in the segmentation process. So the proposed deformable model takes into account not only the gray-level distribution but also a shape model of the kidney that depends on a sign distance map.

A conventional parametric deformable 2D model, or snake, is a curve $\Phi = (\phi(\tau) = (u(\tau), v(\tau); \tau \in T)$ in planar Cartesian coordinates (u, v), where τ is the continuous or discrete index of a contour point, and T is the index range. The deformable model moves through the spatial image domain to minimize the total energy:

$$E = E_{\text{int}} + E_{\text{ext}} = \int_{\tau \in T} \xi_{\text{int}}\big(\phi(\tau)\big) + \xi_{\text{ext}}\big(\phi(\tau)\big) d\tau, \tag{1}$$

where $\xi_{\text{int}}(\phi(\tau))$ and $\xi_{\text{ext}}(\phi(\tau))$ denote the internal and external forces, respectively, that control the pointwise model movements. The total energy is the sum of two terms: the internal energy keeping the deformable model as a single unit and the external one attracting the model to the region boundary. The internal force is typically defined as $\xi_{\text{int}}(\phi(\tau) = \varsigma|\phi'(\tau)|^2 + \kappa|\phi''(\tau)|^2$, where weights ς and κ control the curve's tension and rigidity, respectively, and $\phi'(\tau)$ and $\phi''(\tau)$ are the first and second derivatives of $\phi(\tau)$ with respect to τ.

Typical external forces designed in [57] to lead an active contour toward step edges in a grayscale image $\mathbf{Y}$ are:

$$\xi_{ext}\big(\phi(\tau)\big) = -|\nabla \mathbf{Y}(\phi(\tau))|^2 \text{ or}$$
$$-\big|\nabla\big[G(\phi(\tau)) * \mathbf{Y}(\phi(\tau))\big]\big|^2, \tag{2}$$

where $G(\ldots)$ is a 2D Gaussian kernel and ∇ denotes the gradient operator. But both these and other traditional external forces (e.g., based on lines, edges, or the GVF) fail to make the contour closely approach an intricate boundary with concavities.

Moreover, due to high computational complexity, the deformable models with most of such external energies are slow compared to other segmentation techniques.

As a solution to these problems, we modify the external energy component of this energy formulation, and we formulate an energy function using the density estimations of two distributions: the signed distance map from shape models and the gray-level distribution [58]. The external energy component of our deformable models is formulated as:

$$\xi_{ext}\big(\phi(\tau)\big) = \begin{cases} -p_g(q|k)p_s(d|k) & \text{if} \quad k = k^* \\ p_g(q|k)p_s(d|k) & \text{if} \quad k \neq k^* \end{cases}.$$

In this formulation, k is the region label with $k = 1, 2$, with $k = 1$ denoting the kidney class, $k = 2$ denoting the other tissue, q is the gray level, and d is the signed distance, where $p_s(d|k)$ is the density that describes the signed distance map inside and outside the object, and $p_g(q|k)$ is the density estimation of the gray level. With this energy function, the stochastic external force for each control point $\phi(\tau)$ of the current deformable model evolves in a region k^*. The detailed steps of shape model construction are explained in Section 5.1, and gray-level density estimation is explained in Section 5.2.

5.1. Shape Model Construction

The signed distance map density, $p_s(d|k)$, in the above-mentioned external energy is calculated using a shape model obtained from the images in the data set. The steps to construct this shape model are as follows:

1. Manually segment the objects of interest from the database as shown in Figure 4a,b.

2. Align the images in the training data sets using 2D affine registration (rotation, translation, and scaling) using Mutual Information (MI) [59] as a similarity measure as shown in Figure 4c.

3. Convert aligned images obtained from the previous step to binary images as shown in Figure 4d.

4. Calculate the 2D edge V that describes the boundary of the object for all the manually segmented M number of images obtained in Step 3.

5. From the M number of shapes calculated in Step 3, calculate the signed distance map inside and outside each object. For $m = 1, \ldots, M$, the signed distance map can be calculated as follows:

$$d_m(i, j) = \begin{cases} 0 & (i, j) \in V_i \\ S((i, j), V_m) & (i, j) \in RV_m, \\ -S((i, j), V_m) & \text{Otherwise} \end{cases} \qquad (3)$$

where RV is the region lying inside the kidney shape and $S((i, j), V_m)$ is the minimum Euclidean distance between image location (i, j) and curve V_m. The results of this step are shown in Figure 4e,f.

6. Compute the empirical density of the aligned signed distance maps (Figure 4e) as shown in Figure 4g.

7. Calculate the average signed distance map of the kidney at location (i, j) as:

$$d(i, j) = \frac{1}{M} \sum_{m=1}^{M} d_m(i, j). \tag{4}$$

Then threshold the sign distance map at zero level to obtain an average shape.

8. Average the signed distance maps to obtain an average density estimation of the shape.

Figure 5a shows the average signed distance map for a kidney object. We get the average shape of the kidney by thresholding the signed distance map shown in Figure 5a at zero level, the result of which is shown in Figure 5b. In the same way, we calculate the average empirical densities of the empirical densities shown in Figure 4g, with the result shown in Figure 6. With this approach, all the shape variability is gathered into one density function. Compared to the other approaches such as that of [60], we do not need to conduct a principal component analysis, which is difficult for a big database that contains big images (size 600×600).

Figure 7 evaluates the quality of MI-based affine alignment, with the region maps images being pixelwise averages of all the training maps images, $m = 1, \ldots, M$, before and after mutual alignment of training set M. Similar shapes are significantly overlapped after the alignment, that is, we decrease the variability between shapes.

5.2. Density Estimation

In this section we introduce a new statistical model that approximates an empirical probability density function of scalar data with a linear combination of discrete Gaussians (LCDG) with positive and negative components. Due to both positive and negative components, the LCDG approximates interclass transitions more accurately than a conventional mixture of only positive Gaussians. To estimate the parameters of LCDG, we modify an Expectation-Maximization (EM) algorithm to deal with the LCDG with positive and negative components and also propose a novel EM-based sequential technique to get a close initial LCDG approximation with which the modified EM algorithm should start.
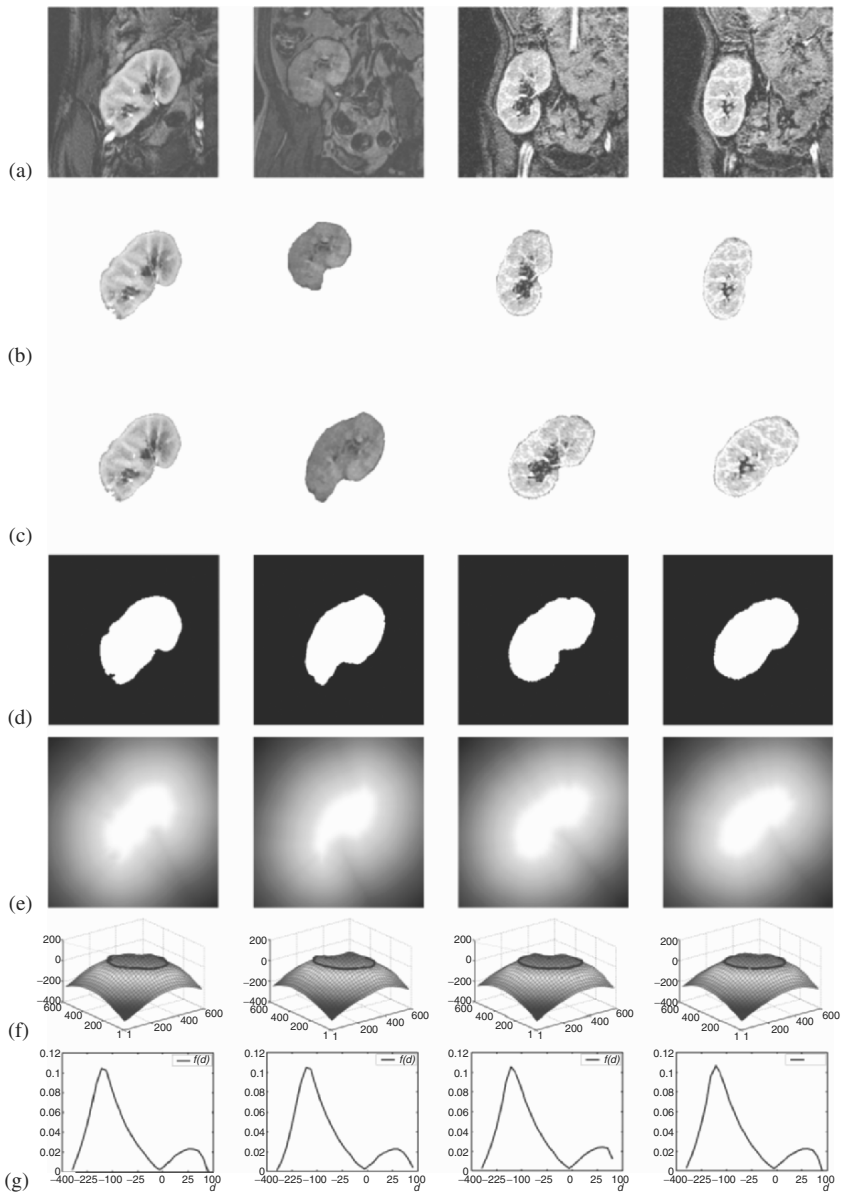
Figure 4. Steps of shape reconstruction. Samples of the database (a), manual segmentation results (b), affine mutual information registration (c), binarization (d), signed distance maps (e), level sets functions (f), and the empirical densities of signed distance maps (g). See attached CD for color version.

(a)   (b)
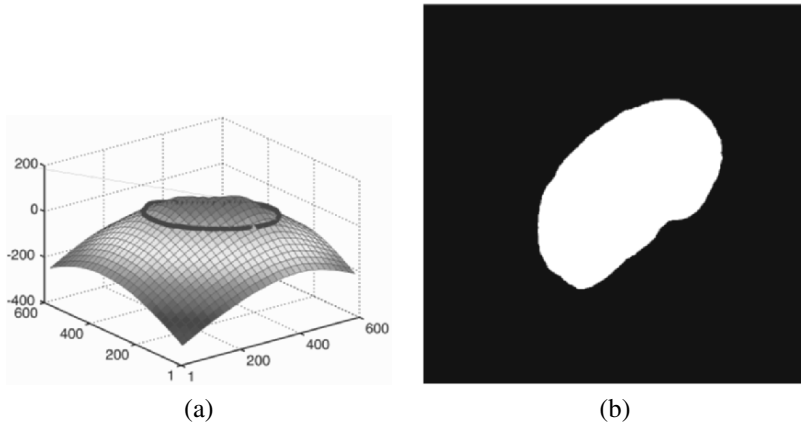
Figure 5. Average signed distance map for the kidney object (a), and the average shape of the kidney after thresholding the average signed distance map from the zero level (b).   See attached CD for color version.
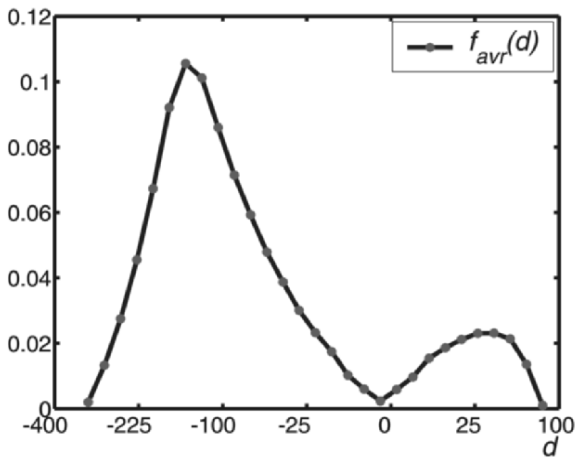
Figure 6. Average empirical signed distance map density representing the shape. It is calculated as the average empirical density of empirical densities shown in Figure 4g. The positive distances indicate the kidney area, while the negative distances indicate the background.

In the following we describe this model to estimate the marginal density for the gray-level distribution $p_g(q)$ in each region. The same approach is used to estimate the density of the signed distances $p_s(d)$ for the object and background.

(a)   (b)
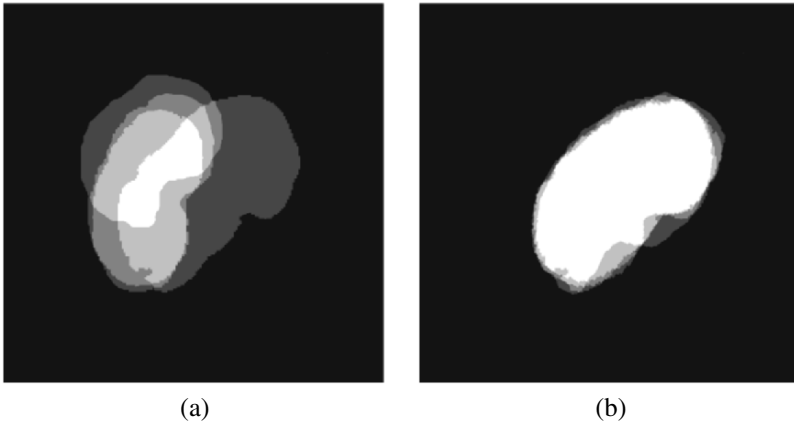
Figure 7. Comparison of the shape overlaps in the training data sets before (a) and after (b) alignment.

Let $\mathbf{Q} = \{0, \ldots, Q\}$ denote sets of gray levels q in the given image. Here, $Q + 1$ is the number of gray levels in the given image. Let $\mathbf{S} = \{(i, j) : 1 \leq i \leq I, 1 \leq j \leq J\}$ be a finite arithmetic grid supporting gray level images $\mathbf{Y} : \mathbf{S} \rightarrow \mathbf{Q}$. The discrete Gaussian (DG) is defined as the discrete probability distribution $\Psi_\theta = (\psi(q|\theta) : q \in \mathbf{Q})$ on $\mathbf{Q}$ such that $\psi(q|\theta) = \Phi_\theta(q + 0.5) - \Phi_\theta(q - 0.5)$ for $q = 1, \ldots, Q - 2$, $\psi(0|\theta) = \Phi_\theta(0.5)$, $\psi(Q - 1|\theta) = 1 - \Phi_\theta(Q - 1.5)$ where $\Phi_\theta(q)$ is the cumulative Gaussian (normal) probability function with a shorthand notation $\theta = (\mu, \sigma^2)$ for its mean, μ, and variance, σ^2.

In contrast to a conventional mixture of Gaussians and/or other simple distributions, one per region, we closely approximate the empirical gray-level distribution for the given image with an LCDG having C_p positive and C_n negative components:

$$p_{g:\mathbf{w},\boldsymbol{\Theta}}(q) = \sum_{r=1}^{C_\mathrm{p}} w_{\mathrm{p},r}\psi(q|\theta_{\mathrm{p},r}) - \sum_{l=1}^{C_\mathrm{n}} w_{\mathrm{n},l}\psi(q|\theta_{\mathrm{n},l}), \tag{5}$$

under the obvious restriction on the weights $\mathbf{w} = [w_{p,.}, w_{n,.}]$:

$$\sum_{r=1}^{C_\mathrm{p}} w_{\mathrm{p},r} - \sum_{l=1}^{C_\mathrm{n}} w_{\mathrm{n},l} = 1. \tag{6}$$

To estimate the parameters for the model given in Eq. (6), we modify the conventional EM algorithm to take into account both positive and negative discrete Gaussian components. The details of the algorithm are described below.

5.3. Modified EM Algorithm for LCDG

Let $\mathbf{F} = [f(q) : q \in \mathbf{Q}]$ be an empirical relative frequency distribution of gray levels q collected over the whole image $\mathbf{Y}$. Assuming independent signals in the pixels $(i, j) \in \mathbf{S}$, the empirical distribution represents an unknown probability density $\psi\psi(q)$ of gray values such that $\int_{-\infty}^{\infty} \psi\psi(q)dq \equiv \sum_{q=0}^{Q} f(q) = 1$. We assume that $\mathbf{F}$ is approximated by an LCDG $\mathbf{P}_{C:\mathbf{w},\boldsymbol{\Theta}} = [p_C(q) : q \in \mathbf{Q}]$ with C_{p} positive and C_{n} negative components $\psi(q|\theta)$:

$$p_{\mathbf{w},\boldsymbol{\Theta}}(q) = \sum_{r=1}^{C_{\mathrm{p}}} w_{\mathrm{p},r} \psi(q|\theta_{\mathrm{p},r}) - \sum_{l=1}^{C_{\mathrm{n}}} w_{\mathrm{n},l} \psi(q|\theta_{\mathrm{n},l}). \tag{7}$$

In line with Eq. (7), the positive weights $\mathbf{w}$ are restricted to unity as shown in Eq. (6):

We also assume here that the numbers C_{p} and C_{n} of the components of each type are known after the initialization in Section 5.4 and do not change during the EM process. The initialization also provides the starting parameter values $\mathbf{w}^{[0]}$ and $\boldsymbol{\Theta}^{[0]}$.

The probability densities form a proper subset of the set of the LCDG due to the additional restriction $p_{\mathbf{w},\boldsymbol{\Theta}}(q) \geq 0$, which holds automatically for probability mixtures with no negative components only. As mentioned earlier, this special feature is ignored because our goal is to closely approximate the empirical data only within the limited range $[0, Q]$. The approximating function of Eq. (7) is assumed strictly positive only in the points $q = 0, 1, \ldots, Q$.

The log-likelihood of the empirical data under the assumed independent signals is as follows:

$$\begin{aligned}
L(\mathbf{w}, \boldsymbol{\Theta}) &= \frac{1}{|\mathbf{S}|} \log \left(\prod_{(i,j) \in \mathbf{S}} f(Y_{i,j}) \right) \\
&= \frac{1}{|\mathbf{S}|} \log \left(\prod_{q \in \mathbf{Q}} (p_{\mathbf{w},\boldsymbol{\Theta}}(q))^{|\mathbf{S}|f(q)} \right) \\
&= \sum_{q \in \mathbf{Q}} f(q) \log p_{\mathbf{w},\boldsymbol{\Theta}}(q).
\end{aligned} \tag{8}$$

The LCDG that provides a local maximum of the log-likelihood in Eq. (8) can be found using the iterative block relaxation process extending the conventional scheme in [61] that was proposed initially in [62].

Let

$$p_{\mathbf{w},\boldsymbol{\Theta}}^{[m]}(q) = \sum_{r=1}^{C_{\mathrm{p}}} w_{\mathrm{p},r}^{[m]} \psi(q|\theta_{\mathrm{p},r}^{[m]}) - \sum_{l=1}^{C_{\mathrm{n}}} w_{\mathrm{n},l}^{[m]} \psi(q|\theta_{\mathrm{n},l}^{[m]})$$

be the LCDG at step, or iteration, m. Relative contributions of each data item $q = 0, \ldots, Q$ into each positive and negative Gaussian at the step m are specified by the respective conditional weights:

$$
\pi_{\mathrm{p}}^{[m]}(r|q) = \frac{w_{\mathrm{p},r}^{[m]} \psi(q|\theta_{\mathrm{p},r}^{[m]})}{p_{\mathbf{w},\boldsymbol{\Theta}}^{[m]}(q)}; \quad \pi_{\mathrm{n}}^{[m]}(l|q) = \frac{w_{\mathrm{n},l}^{[m]} \psi(q|\theta_{\mathrm{n},l}^{[m]})}{p_{\mathbf{w},\boldsymbol{\Theta}}^{[m]}(q)}, \tag{9}
$$

such that the following condition holds:

$$
\sum_{r=1}^{C_{\mathrm{p}}} \pi_{\mathrm{p}}^{[m]}(r|q) - \sum_{l=1}^{C_{\mathrm{n}}} \pi_{\mathrm{n}}^{[m]}(l|q) = 1; \quad q = 0, \ldots, Q. \tag{10}
$$

Multiplying the right-hand side of Eq. (8) by the left-hand side of Eq. (10), which is valid since this latter has unit value, the log-likelihood of Eq. (8) can be rewritten in the equivalent form:

$$
\begin{aligned}
L(\mathbf{w}^{[m]}, \boldsymbol{\Theta}^{[m]}) \quad &= \quad \sum_{q=0}^{Q} f(q) \left[\sum_{r=1}^{C_{\mathrm{p}}} \pi_{\mathrm{p}}^{[m]}(r|q) \log p_{\mathbf{w},\boldsymbol{\Theta}}^{[m]}(q) \right] \\
&\quad - \sum_{q=0}^{Q} f(q) \left[\sum_{l=1}^{C_{\mathrm{n}}} \pi_{\mathrm{n}}^{[m]}(l|q) \log p_{\mathbf{w},\boldsymbol{\Theta}}^{[m]}(q) \right].
\end{aligned} \tag{11}
$$

The next equivalent form more convenient for specifying the block relaxation process is obtained after replacing $\log p_{\mathbf{w},\boldsymbol{\Theta}}^{[m]}(q)$ in the first and second brackets with the equal terms: $\log w_{\mathrm{p},r}^{[m]} + \log \psi(q|\theta_{\mathrm{p},r}^{[m]}) - \log \pi_{\mathrm{p}}^{[m]}(r|q)$ and $\log w_{\mathrm{n},l}^{[m]} + \log \psi(q|\theta_{\mathrm{n},l}^{[m]}) - \log \pi_{\mathrm{n}}^{[m]}(l|q)$, respectively, which follow directly from Eq. (9).

The block relaxation converges to a local maximum of the likelihood function in Eq. (11) by repeating iteratively the following two steps of conditional maximization (comprising the E-step and the M-step, respectively [61]):

1. Find the conditional weights of Eq. (9) by maximizing the log-likelihood $L(\mathbf{w}, \boldsymbol{\Theta})$ under the fixed parameters $\mathbf{w}^{[m]}, \boldsymbol{\Theta}^{[m]}$ from the previous iteration m, and

2. Find the parameters $\mathbf{w}^{[m+1]}, \boldsymbol{\Theta}^{[m+1]}$ by maximizing $L(\mathbf{w}, \boldsymbol{\Theta})$ under the fixed conditional weights of Eq. (9)

until the changes of the log-likelihood and all the model parameters become small.

The first step performing the conditional Lagrange maximization of the log-likelihood of Eq. (11) under the $Q + 1$ restrictions of Eq. (10) results just in the conditional weights $\pi_{\mathrm{p}}^{[m+1]}(r|q)$ and $\pi_{\mathrm{n}}^{[m+1]}(l|q)$ of Eq. (9) for all $r = 1, \ldots, C_{\mathrm{p}}$; $l = 1, \ldots, C_{\mathrm{n}}$ and $q = 0, \ldots, Q$.

The second step performs conditional Lagrange maximization of the log-likelihood of Eq. (11) under the restriction of Eq. (6). It results in the conditional mathematical expectations of the model parameters involving the fixed conditional weights of Eq. (9) as conditional probabilities. The expected weights $\mathbf{w}^{[m+1]}$ at the second step conform to:

$$
\begin{aligned}
w_{\mathrm{p},r}^{[m+1]} &= \sum_{q \in \mathbf{Q}} f(q)\pi_{\mathrm{p}}^{[m+1]}(r|q) \\
w_{\mathrm{n},l}^{[m+1]} &= \sum_{q \in \mathbf{Q}} f(q)\pi_{\mathrm{n}}^{[m+1]}(l|q)
\end{aligned}
\quad .
$$

The expected parameters $\Theta^{[m+1]}$ of each Gaussian have conventional forms that follow from the unconditional maximization of the log-likelihood of Eq. (11):

$$
\mu_{\mathrm{c},r}^{[m+1]} = \frac{1}{w_{\mathrm{c},r}^{[m+1]}} \sum_{q \in \mathbf{Q}} q f(q)\pi_{\mathrm{c}}^{[m+1]}(r|q)
$$

$$
(\sigma_{\mathrm{c},r}^{[m+1]})^2 = \frac{1}{w_{\mathrm{c},r}^{[m+1]}} \sum_{q \in \mathbf{Q}} \left(q - \mu_{\mathrm{c},i}^{[m+1]}\right)^2 f(q)\pi_{\mathrm{c}}^{[m+1]}(r|q).
$$

where c stands for p or n, respectively.

This modified EM algorithm is valid while the weights of Eq. (9) are strictly positive, and the initial LCDG approximation should comply with this limitation. The iterations have to be terminated when the log-likelihood of Eq. (11) begins to decrease. Generally, if the initialization is incorrect, this algorithm may diverge from the very beginning. Thus, the initial LCDG has to closely approximate the empirical distribution.

5.4. Sequential EM-Based Initialization

We assume that the number of dominant modes is equal to the given number of classes. To simplify the notation, let the empirical distribution have only two separate dominant modes representing the object (kidney) and the background, respectively, since we have only two classes for this specific problem. The algorithm we present below is easily extended to the general case of $K > 2$ dominant modes. We assume that each dominant mode is roughly approximated with a single Gaussian and the deviations of the empirical density from the two-component dominant Gaussian mixture are described by other components of the LCDG in Eq. (5). Therefore, the model has the two dominant positive weights, say, $w_{\mathrm{p},1}$ and $w_{\mathrm{p},2}$ such that $w_{\mathrm{p},1} + w_{\mathrm{p},2} = 1$, and a number of "subordinate" weights of smaller absolute values such that $\sum_{r=3}^{C_{\mathrm{p}}} w_{\mathrm{p},r} - \sum_{l=1}^{C_{\mathrm{n}}} w_{\mathrm{n},l} = 0$.

The following sequential algorithm allows for estimating both the weights and parameters of the individual Gaussians in the previous LCDG model, including the number of the non-dominant components:

1. Approximate a given empirical distribution $\mathbf{F}$ of gray levels in the image $\mathbf{Y}$ with a dominant mixture $\mathbf{P}_2$ of two Gaussians using the conventional EM algorithm.

2. Find the deviations $\mathbf{\Delta} = [\Delta(q) = f(q) - p_2(q) : q \in \mathbf{Q}]$ between $\mathbf{F}$ and P_2 and split them into the positive and negative parts such that $\delta(q) = \delta_p(q) - \delta_n(q)$:

$$
\begin{aligned}
\mathbf{\Delta}_p &= [\delta_p(q) = \max\{\delta(q), 0\} : q \in \mathbf{Q}\], \\
\mathbf{\Delta}_n &= [\delta_n(q) = \max\{-\delta(q), 0\} : q \in \mathbf{Q}\].
\end{aligned}
\tag{12}
$$

3. Compute the scaling factor for the deviations: $Scale = \int\limits_{-\infty}^{\infty} \delta_p(q)dq \equiv \int\limits_{-\infty}^{\infty} \delta_n(q)dq.$

4. If the factor $Scale$ is less than an accuracy threshold, terminate and return the model $\mathbf{P}_C = \mathbf{P}_2$.

5. Otherwise, consider the scaled-up absolute deviations $\frac{1}{Scale}\mathbf{\Delta}_p$ and $\frac{1}{Scale}\mathbf{\Delta}_n$ as two new "empirical densities" and use iteratively the conventional EM algorithm to find sizes C_p and C_n of the Gaussian mixtures, $\mathbf{P}_p$ and $\mathbf{P}_n$, respectively, approximating the best scaled-up deviations.

   (a) The size of each mixture corresponds to the minimum of the integral absolute error between the scaled-up absolute deviation $\mathbf{\Delta}_p$ (or $\mathbf{\Delta}_n$) and its model $\mathbf{P}_p$ (or $\mathbf{P}_n$). The number of components is increasing sequentially by a unit step while the error is decreasing.

   (b) Due to multiple local maxima, such a search may be repeated several times with different initial parameter values in order to select the best approximation.

6. Scale down the subordinate models $\mathbf{P}_p$ and $\mathbf{P}_n$ (i.e., scale down the weights of their components) and add the scaled model $\mathbf{P}_p$ to and subtract the scaled model P_n from the dominant model $\mathbf{P}_2$ in order to form the desired model $\mathbf{P}_C$ of the size $C = 2 + C_p + C_n$.

Since the EM algorithm converges to a local maximum of the likelihood function, it may be repeated several times with different initial parameter values for choosing the model that yields the best approximation. In principle, this process can be repeated iteratively in order to approximate more and more closely the residual absolute deviations between $\mathbf{F}$ and $\mathbf{P}_C$. But because each Gaussian in the latter model impacts all the values $p(q)$, the iterations should be terminated when the approximation quality begins to decrease.

We use the Levy distance [63], $\rho(\mathbf{F}, \mathbf{P})$, between the estimated model $\mathbf{P}$ and the empirical distribution $\mathbf{F}$ to evaluate the approximation quality. The distance is defined as the minimum positive value α such that the two-sided inequalities $p(q - \alpha) - \alpha \le f(q) \le p(q + \alpha) + \alpha$ hold for all $q \in \mathbf{Q}$:

$$\rho(\mathbf{F}, \mathbf{P}) = \min_{\alpha > 0}\{\alpha : p(q - \alpha) - \alpha \le f(q) \le p(q + \alpha) + \alpha \ \ \forall q \in \mathbf{Q}\}. \quad (13)$$

It has been proven [63] that model $\mathbf{P}$ weakly converges to $\mathbf{F}$ when $\rho(\mathbf{F}, \mathbf{P}) \to 0$. Our experiments show that the modified EM algorithm typically decreases an initially large Levy distance between the empirical distribution and its estimated model to a relatively small value.

5.5. Classification of the Model Components

The final mixed LCDG model P has to be split into K LCDG submodels, one per class, by associating each subordinate component with a particular dominant term in such a way as to minimize the expected misclassification rate. To illustrate the association principle, let us consider the bimodal case with the two dominant Gaussians having the mean values μ_1 and μ_2; $0 < \mu_1 < \mu_2 < Q$. Let all the subordinate components be ordered by their mean values, as well. Then those with mean values smaller than μ_1 and greater than μ_2 relate to the first and second class, respectively. The components having the mean values in the range $[\mu_1, \mu_2]$ are associated with the classes by simple thresholding such that the means below the threshold, t, belong to the components associated with the first class. The desired threshold minimizes the classification error $e(t)$:

$$e(t) = \int_{-\infty}^{t} p(q|2)dq + \int_{t}^{\infty} p(q|1)dq. \quad (14)$$

To make our approach of density estimation clear, we will discuss step-by-step density estimation for the mixed empirical density of the average signed distance map of the kidney object. Figure 8a shows the initial step of the bimodal empirical distribution of signed distance map in Figure 6. The dominant modes represent the brighter kidney area and its background, respectively. Figure 8b shows the deviation and absolute deviation between the two dominant modes and the empirical density. Figure 8c–f shows the final DG mixtures; the initial mixed LCDG model consists of the 2 dominant, 3 additive, and 4 subtractive DGs, that is, $C_{\mathrm{p}} = 5$ and $C_{\mathrm{n}} = 4$. Figure 8f shows that our modified EM algorithm converges after the 16 first iterations of the refinement before the process terminates and increases the log-likelihood from -6.18 for the initial LCDG to -5.10.
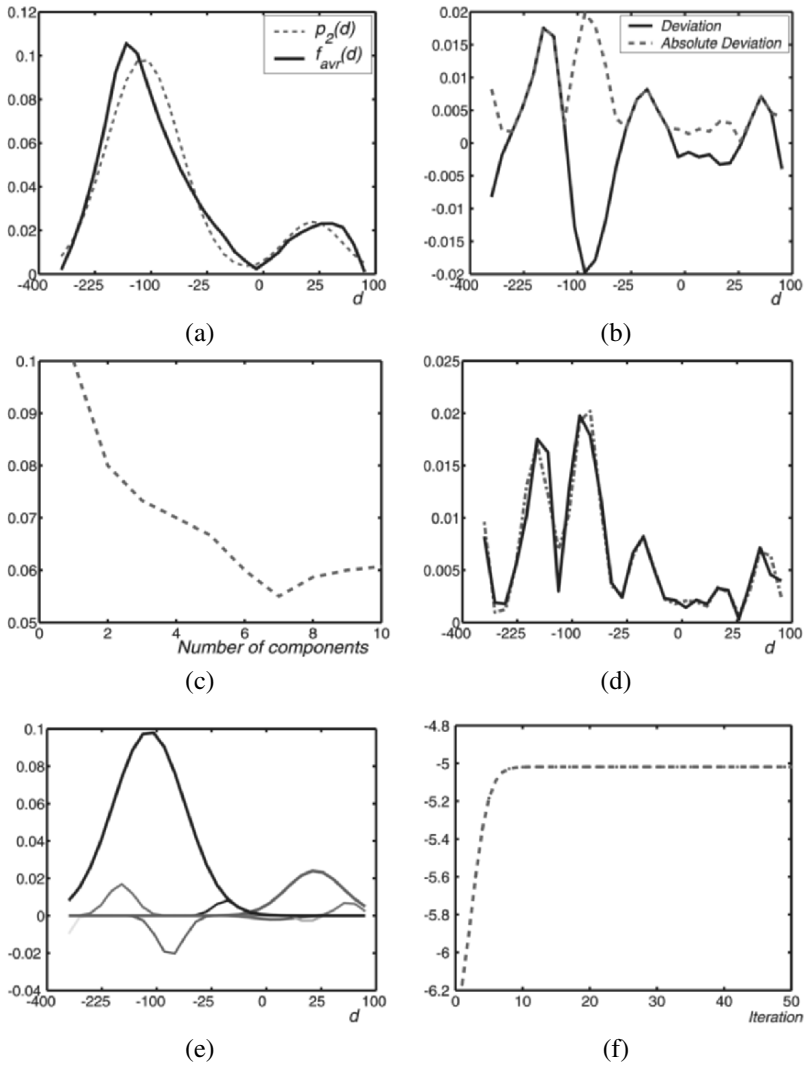
Figure 8. Estimated two dominant modes that present the kidney area and its background (a); the scaled-up absolute deviation of the approximation and its LCDG model (b); approximation error for the scaled absolute deviation as a function of number of subordinate Gaussians (c); density estimation of the scaled-up absolute deviation (d); final LCDG model (e); and log-likelihood changes at the EM iterations (f).

(a)   (b)
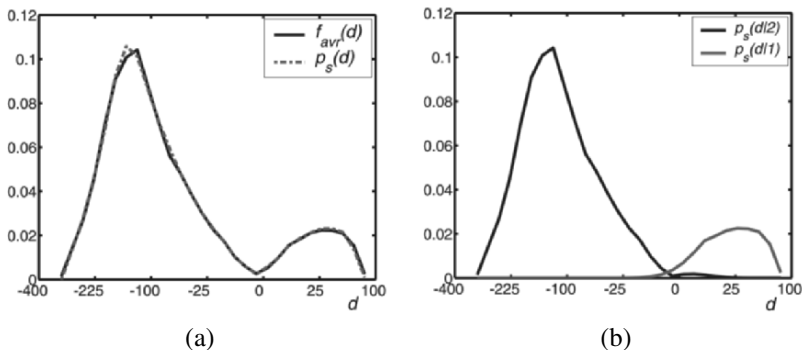
Figure 9. Final two-class LCDG approximation of the mixed density (a); and final LCDG models for each class (b).

Figure 9 presents the final estimated density using the LCDG model for both mixed density and the marginal density for each class. In Figure 9a the Levy distance between the empirical density and the estimated density is 0.008, which indicates a good match between the empirical distribution and the estimated one.

It is important to note that this shape density is calculated only once; then it is used as it is during kidney segmentation of all other given abdomen images.

5.6. Stepwise Deformable Model Algorithm and Segmentation Results

For any given image, the proposed algorithm of segmenting the region k^* is as follows:

1. Register the given image to one of the aligned images in the database using 2D affine registration based on using mutual information as a similarity measure. This step makes the algorithm invariant to scaling, rotation, or translation.

2. Use the modified EM algorithm to estimate the parameters of the LCDG density model for signed distance map $p_s(d|k)$ inside and outside the object of interest from the average shape which was calculated a priori.

3. Calculate the normalized histogram for the given image.

4. Use the modified EM algorithm to estimate the parameters of the LCDG density model for each class $p_g(q|k)$, k being the class number $k = 1...K$.

5. Initialize the control points $\phi(\tau)$ for the deformable model, and for each control point $\phi(\tau)$ on the current deformable model, calculate sign dis-
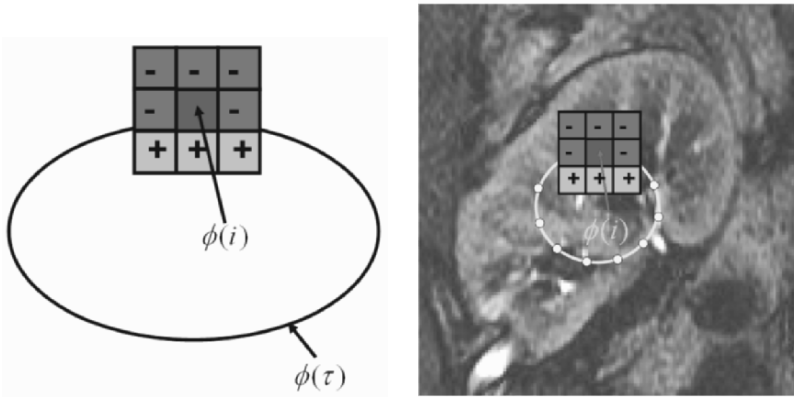
Figure 10. Greedy propagation of the deformable model (a). The deformable model in (a) is initialized in the given kidney to be segmented (b). See attached CD for color version.

tances indicating exterior $(-)$ or interior $(+)$ positions of each of the eight nearest neighbors w.r.t. the contour as shown in Figure 10.

6. Check the label k for each control point:

    (a) If the point is assigned to the region $k = k^*$, then

        i. Estimate the region labels for its neighbors using a Bayesian classifier such that they have the $(-)$ distance.

        ii. If some of these sites are also assigned to the class k^*, then move the control point to the neighboring position ensuring the minimum total energy (i.e., expand the contour).

        iii. Otherwise, do not move this point (the steady state).

    (b) If the point is assigned to the region $k \neq k^*$, then

        i. Estimate the region labels for its neighbors using a Bayesian classifier such that they have the $(+)$ distance.

        ii. Move the control point to the neighboring position ensuring the minimum total energy (i.e., contract the contour).

7. If the iteration adds new control points, use the bicubic interpolation of the whole contour and then smooth all its control points with a lowpass filter.

8. Repeat steps 6 and 7 until no positional changes in the control points occur.

The first step of our approach is to estimate the density from the given image for both the kidney object and its background. Unlike the shape density estimation,

the gray-level density estimation step will be repeated for every image we need to segment; so that our approach is adaptable for all data.

Figure 11 shows the initial approximation of the bimodal empirical distribution of $Q = 256$ gray levels over a typical DCE-MRI (Dynamic Contrast-Enhanced Magnetic Resonance Imaging) slice of human abdomen. The dominant modes represent the brighter kidney area and its darker background, respectively. After the additive and subtractive parts of the absolute deviation are approximated with the DG mixtures, the initial mixed LCDG model consists of the 2 dominant, 4 additive, and 4 subtractive DGs, that is, $C_p = 6$ and $C_n = 4$. The LCDG models of each class are obtained with $t = 78$, ensuring the best class separation.

Figure 12 presents the final LCDG model obtained by refining the above initial one using the modified EM algorithm introduced in Section 5.3. The first 37 iterations of the algorithm increase the log-likelihood of Eq. (11) from -6.90 to -4.49. Also, the Levy distance between the empirical density and the estimated density is 0.007, which indicates a good match between the empirical distribution and the estimated one.

The second step of the proposed approach is the alignment step. Figure 13a demonstrates one of our aligned databases. Figure 13b shows one kidney image that we need to segment. Figure 13c shows the result of the registration of (a) and (b) using MI. Figure 14 shows the final steps of the proposed approach. The resulting segmentation in Figure 14c has an error of 0.23% with respect to radiologist segmentation (ground truth). Figure 15 shows another example of kidney segmentation using the proposed approach. To highlight the accuracy of the proposed approach, we compared the proposed approach with the more conventional geometric deformable model presented in [60], where the level set-based shape prior gives an error of 4.9% (Figure 15g). Similar results for four other kidney images in Figure 16 suggest that the latter approach fails to detect sizeable fractions of the goal objects.

In the above examples, the abdominal images were from different patients to show the applicability of our approach, and also to demonstrate the difficulty of the problem. From here on, we will be using the images of only one patient to illustrate the steps of our approach. The segmentation results of one patient are given in Figure 17, a part of whose sequence was given in Figure 2.

## 6. MODEL FOR THE LOCAL DEFORMATION

In DCE-MRI sequences, the registration problem arises because of patient movement and breathing. To overcome this problem, we proposed a new approach to handle kidney motion. The proposed approach is based on deforming the segmented kidney over closed equispaced contours (i.e., isocontours) to closely match the prototype. We did not use a free-form deformation based on a B-spline on a square lattice because that requires additional smoothing constraints that lead

(a)   (b)

(c)   (d)
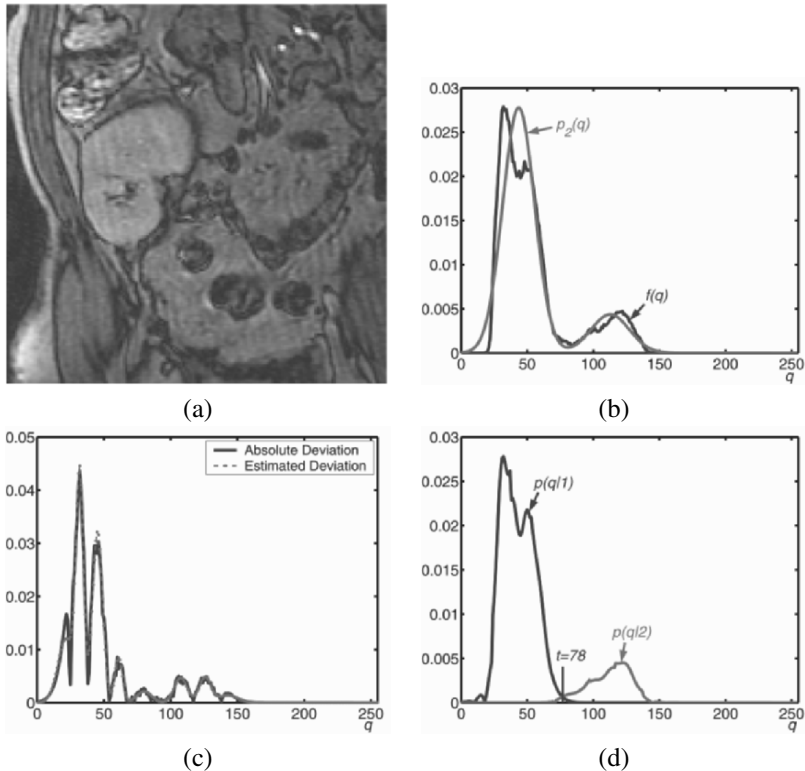
Figure 11. Initial LCDG model of the bimodal empirical gray-level distribution: the DMRI
slice (a), its empirical gray-level distribution approximated with the dominant mixture of
the DGs (b), the scaled-up absolute deviation of the approximation and its LCDG model
(c), and the LCDG model of each class (d) for the best separating threshold $t = 78$. See
attached CD for color version.

to very time-consuming computations. Instead we used evolution of the isocon-
tours guided with an exponential speed function in the directions that minimize
the distances between corresponding pixel pairs on the isocontours of both the
objects. The normalized cross-correlation is used as an image similarity measure
insensitive to intensity changes (e.g., due to tissue motion in medical imagery and
the contrast agent).

The first step of the proposed approach is to use the fast marching level set
methods [46] to generate the distance map inside the kidney regions, as shown in
Figure 18a,b. The second step is to use this distance map to generate equally spaced
separated contours (isocontours) as shown in Figure 18c,d. Note that the number
of isocontours depends on the accuracy and speed that the user needs to achieve.
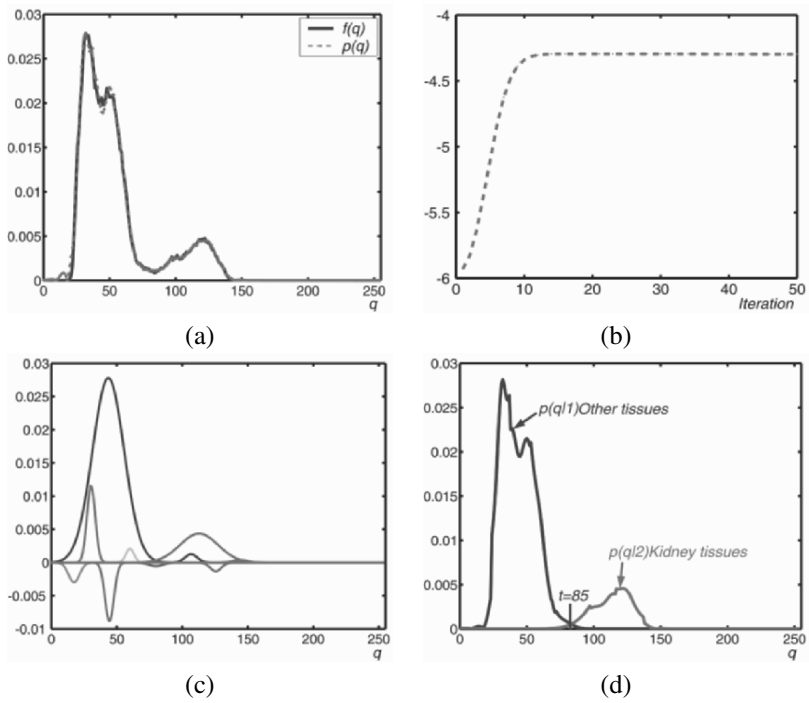
Figure 12. Final 2-class LCDG model (a), log-likelihood changes at the EM iterations (b), ten components of the final LCDG (c), the final LCDG model of each class for the best separating threshold $t = 85$ (d). See attached CD for color version.
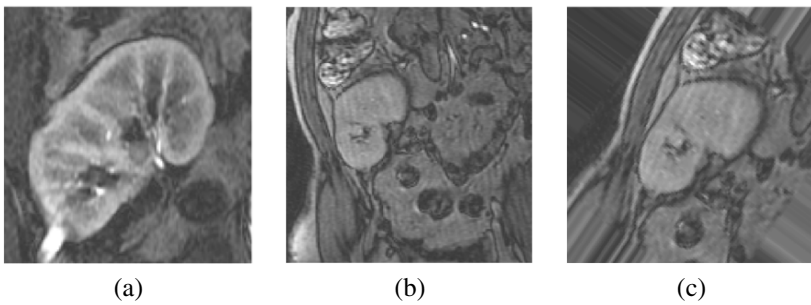

Figure 13. Kidney from the aligned database (a); a kidney to segment (b); alignment of (a) and (b) using affine mutual information registration (c).
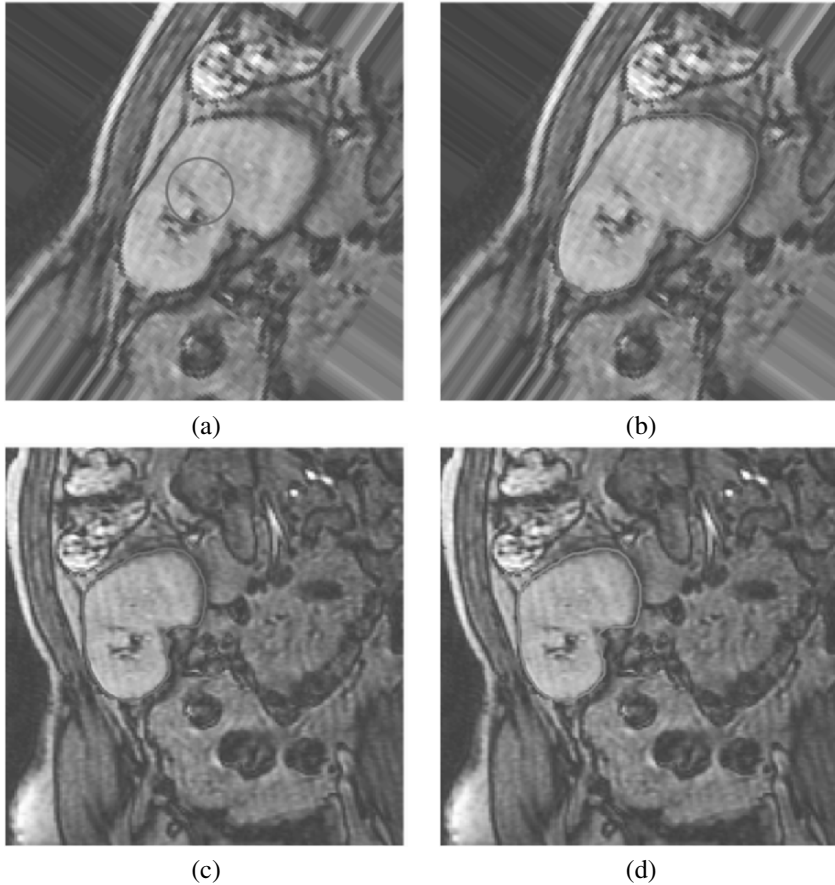
Figure 14. Initialization of deformable model (a); final segmentation of the aligned image (b); final segmentation (c) after multiplying the aligned image by inverse transformation (error = 0.23%); and radiologist segmentation (d).   See attached CD for color version.

The third step of the proposed approach is to use normalized cross-correlation to find the correspondence between isocontours. Since we start with aligned images, we limit our searching space to a small window (e.g., 10×10) to improve the speed of the proposed approach. The final step is evolution of the isocontours. Here our goal is to deform the isocontours in the first (target) image to match the isocontours in the second (source) image. Before we discuss the details of the evolution algorithm, let us define the following terminology:
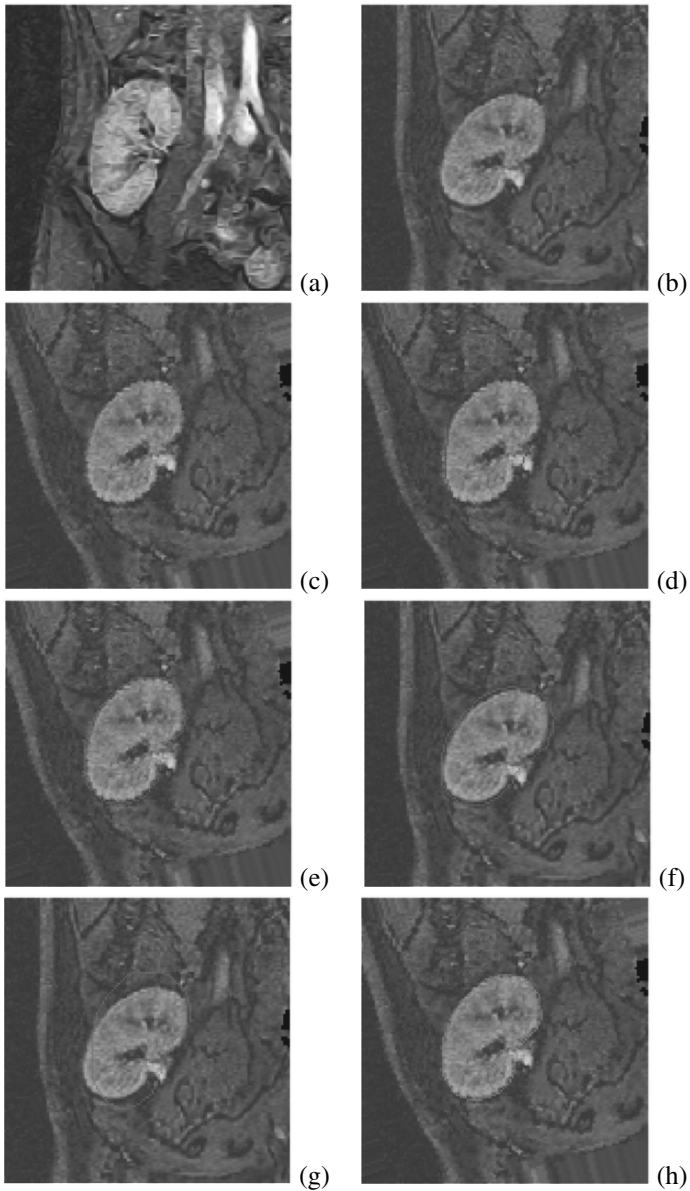
Figure 15. Chosen training kidney prototype (a); an image to be segmented (b); its alignment to the prototype (c); the contour of the training prototype superimposed on the aligned test image (d); the segmentation result (e); the same result (f) after its inverse affine transform to the initial image (b) (total error 0.63% in comparison to ground truth (h); the final boundary and the ground truth are in red and green, respectively), and the segmentation (g) with the algorithm in [60] (the total error 4.9% in comparison to ground truth (h)). See attached CD for color version.

Error 0.67%   Error 4.1%

Error 1.5%   Error 7.4%

Error 1.5%   Error 6.4%

Error 1.3%   Error 5.9%
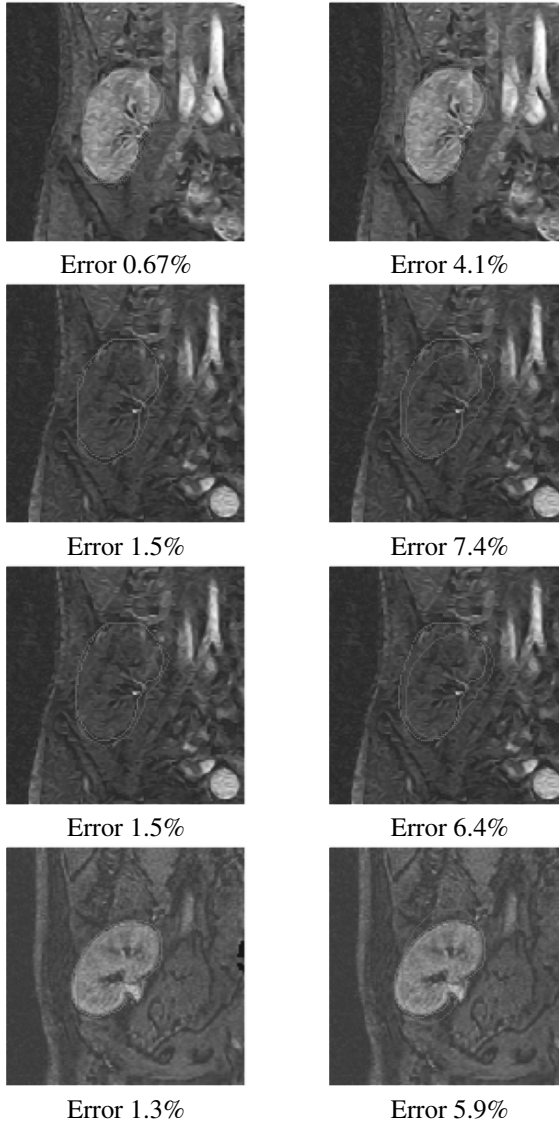
Figure 16. Segmentation of four other kidney DCE-MR images: the left column — our final boundaries and the ground truth (in red and green, respectively); the right column — the segmentation with the algorithm in [60] vs. the ground truth (in red and green, respectively). See attached CD for color version.
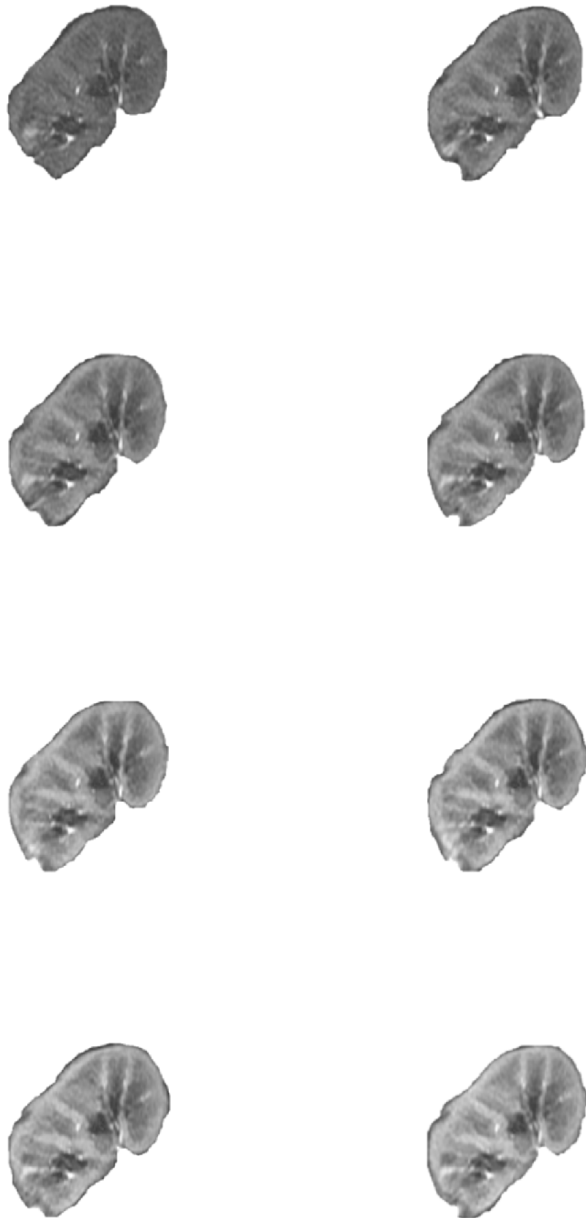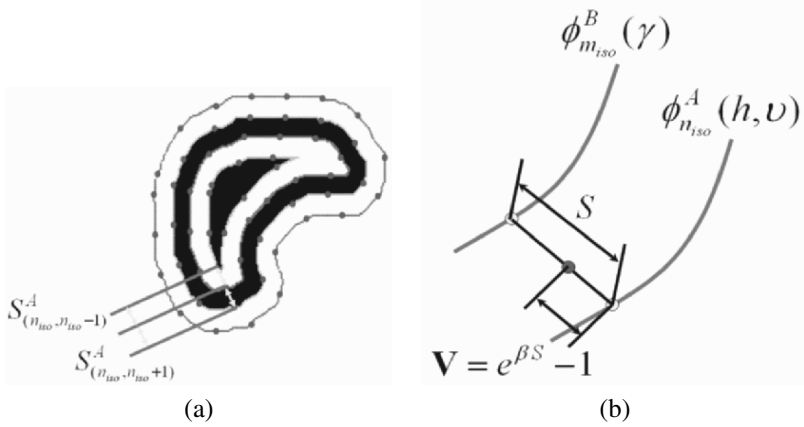
Figure 17. Segmentation results of a DCE-MRI series, a part of which was shown in Figure 2.

(a)   (b)

(c)   (d)
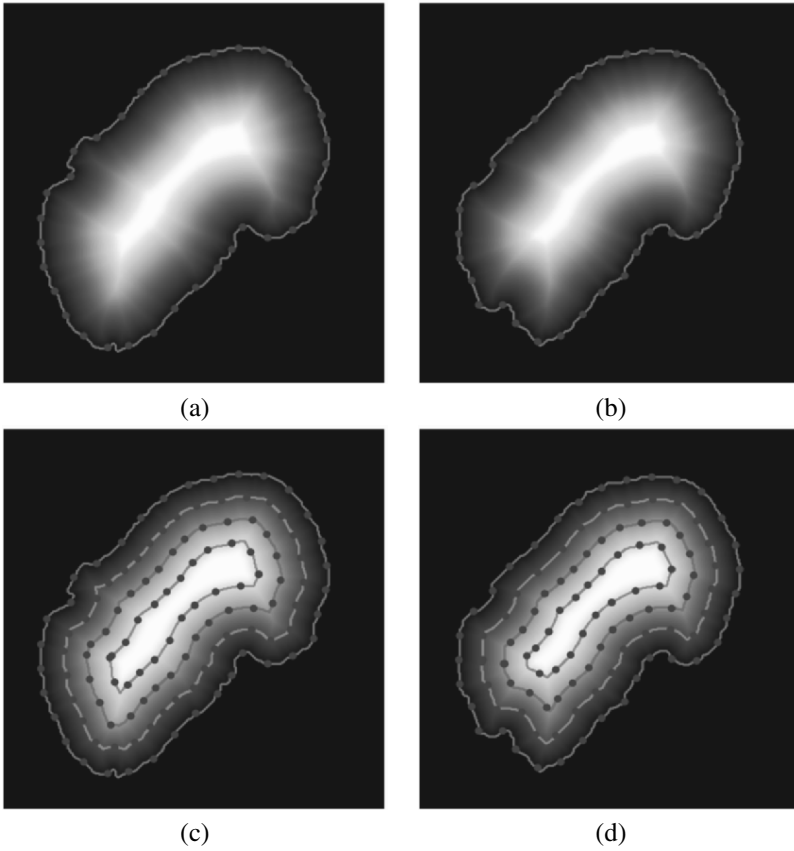
Figure 18. Distance map of two kidneys (a, b) and the samples of isocontours (c, d). See attached CD for color version.

- $\phi^A_{n_{\text{iso}}}(h, \nu)$ are the isocontours in the target image, where $h = 1, \ldots, \mathcal{H}$ is the index of the control points in the given contour, $n_{\text{iso}} = 1, \ldots N_{\text{iso}}$ is the index of the isocontours, and ν is the iteration step.

- $\phi^B_{m_{\text{iso}}}(\gamma)$ are the isocontours in the source image, where $\gamma = 1, \ldots, \Gamma$ is the index of control points in the given contour, and $m_{\text{iso}} = 1, \ldots, M_{\text{iso}}$ is the index of the isocontours.

- S is the Euclidean distance between corresponding points located on both isocontours of both images.

- $S^A_{n_{\text{iso}}, n_{\text{iso}}-1}$ is the Euclidian distance between $\phi^A_{n_{\text{iso}}}(l, \nu)$ and $\phi^A_{n-1}(l, \nu)$.

- $\mathbf{V}$ is the propagation speed function.

Figure 19. Model constraints (a), and model evolution (b). See attached CD for color version.

The most important step in model propagation is selection of propagation speed function $\mathbf{V}$. Selection of the speed function must satisfy the following conditions:

1. $\mathbf{V} = 0$ if $S = 0$.

2. $\mathbf{V} \leq \min(S, S^A_{n_{\mathrm{iso}}, n_{\mathrm{iso}}-1}, S^A_{n_{\mathrm{iso}}, n_{\mathrm{iso}}+1})$ if $S > 0$; is the smoothness constraint, which prevents the current point from passing the closest neighbor contour, as shown in Figure 19.

A speed function of the following form satisfies the above conditions:

$$\mathbf{V} = e^{\beta S} - 1, \tag{15}$$

where β is the propagation constant with the upper bound

$$\beta \preceq \frac{\ln\left(\min(S, S^A_{n_{\mathrm{iso}}, n_{\mathrm{iso}}-1}, S^A_{n_{\mathrm{iso}}, n_{\mathrm{iso}}+1}) + 1\right)}{S}.$$

Based on the speed function shown in Eq. (15) we can deform the isocontours using the following equation, as shown in Figure 19b:

$$\phi^A(h, \nu+1) = \frac{\mathbf{V}}{S}\phi^B_{m_{\mathrm{iso}}}(\gamma) + \frac{S-\mathbf{V}}{S}\phi^A_{n_{\mathrm{iso}}}(h, \nu) \tag{16}$$

for $h = 1, \ldots, \mathcal{H}$, $m_{\mathrm{iso}} = 1, \ldots, M_{\mathrm{iso}}$, $n_{\mathrm{iso}} = 1, \ldots, N_{\mathrm{iso}}$.

To show the quality of the proposed approach, we fused the two kidney images by means of the checkerboard visualization in Figure 20. It is clear from Figure 20b that the connectivity between the two images at the edges and inside the kidney region are improved after applying the proposed deformation model.
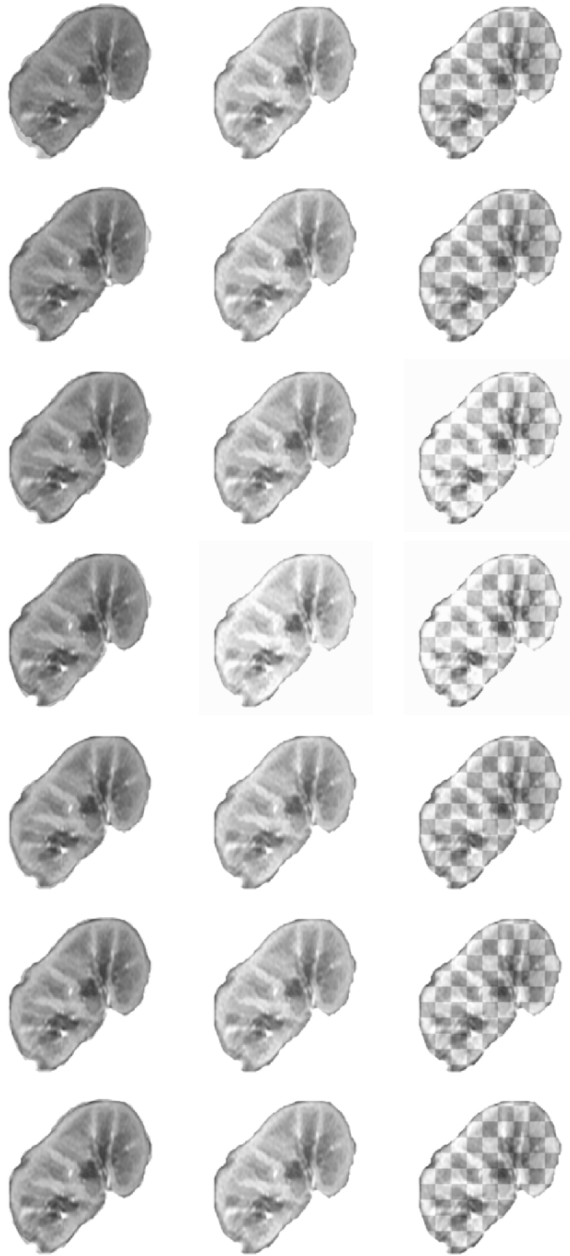
**Figure 20.** Example of a DCE-MRI series after nonrigid registration.

7. CORTEX SEGMENTATION

Strake et al. [64] have shown that the most important signal characteristics come from the cortex of the kidney during acute rejection. Therefore, the final step of our approach is to segment the cortex from the segmented kidney. To achieve this task, we use the same approach but based now only on intensity. At this step, since all the kidneys are aligned together, we select seed points from the medulla regions, and evolve our deformable model based only on intensity. After we extract the medullary regions, the rest is cortex, which is used as a mask and propagated over the whole sequence to plot the average cortex intensity. In Figure 21 we show the cortex segmentation results. In Figure 21a we manually initialize several deformable models inside the medullar regions, and we allow our deformable model evolve in these regions with gray-level information as shown in Figure 21b. The cortex mask is applied to the rest of the sequence as shown in Figure 21c–h.

8. RESULTS

The ultimate goal of the proposed algorithms is to successfully construct a renogram (mean signals) from DCE-MRI sequences, showing the behavior of the kidney as the contrast agent perfuses through the transplanted organ. In acute rejection patients, the DCE-MRI images show a delayed perfusion pattern and reduced cortical enhancement. We tested the above algorithms on thirty patients, four of which are shown in Figure 22. The normal patient shows the expected abrupt increase to higher signal intensities and the dip with a small slope. The acute rejection patients show a delay in reaching peak signal intensities. From these observations we have been able to conclude that the relative peak signal intensity, the time to peak signal intensity, the slope between the peak and the first minimum, and the slope between the peak and the signal measured from the last image in the sequence are the four major features in the renograms of the segmented kidney undergoing classification.

To distinguish between normal and acute rejection, we used a Bayesian supervised classifier, learning statistical characteristics from a training set for normal and acute rejection. The density estimation required in the Bayes classifier is performed for each feature by using a linear combination of Gaussians (LCDG) with positive and negative components, and their parameters are estimated using a modified EM algorithm that appeared in [65]. In our approach we used 50% of the data for training and the other 50% for testing. For testing data the Bayes classifier succeeded in classifying 13 of 15 correctly (86.67%). For the training data the Bayes classifier classified all of them correctly, so the overall accuracy of the proposed approach is 93.3%. All these values were calculated with respect to biopsy results.
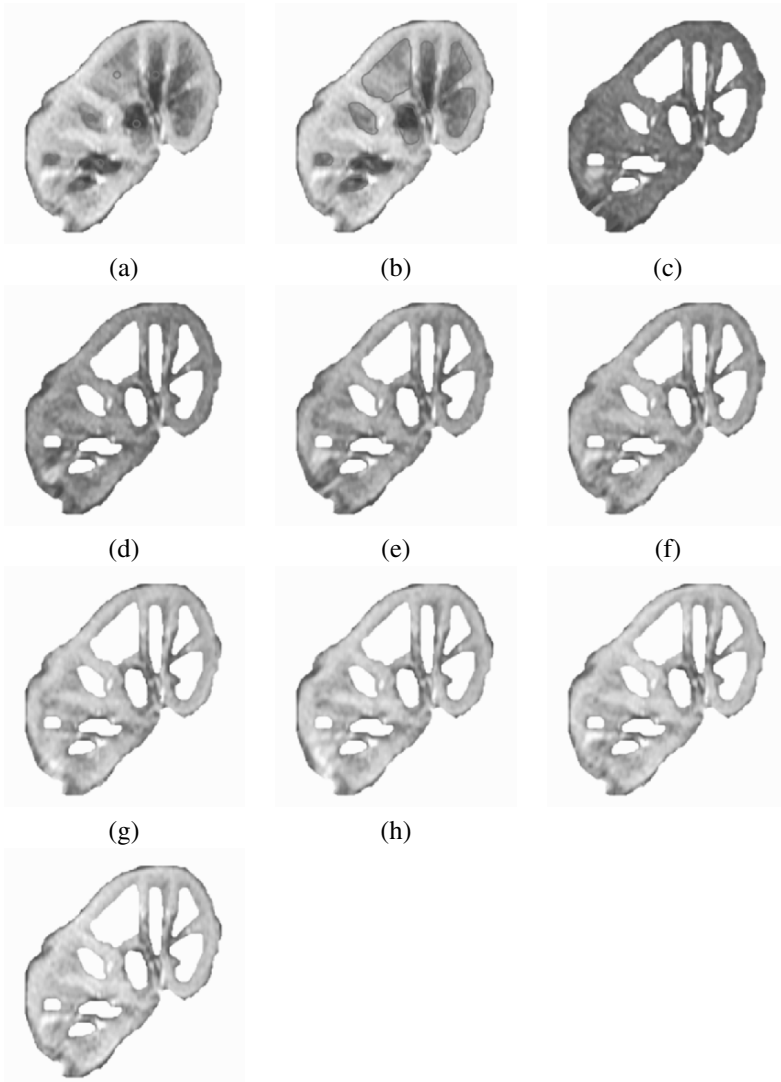
Figure 21. Segmentation of the cortex from kidney images. Several medullary seeds are initialized (a), and the deformable model grows from these seed points (b). After the medulla is extracted from the kidney, the cortex is propagated over the whole sequence of images, as shown in (c)-(h). See attached CD for color version.
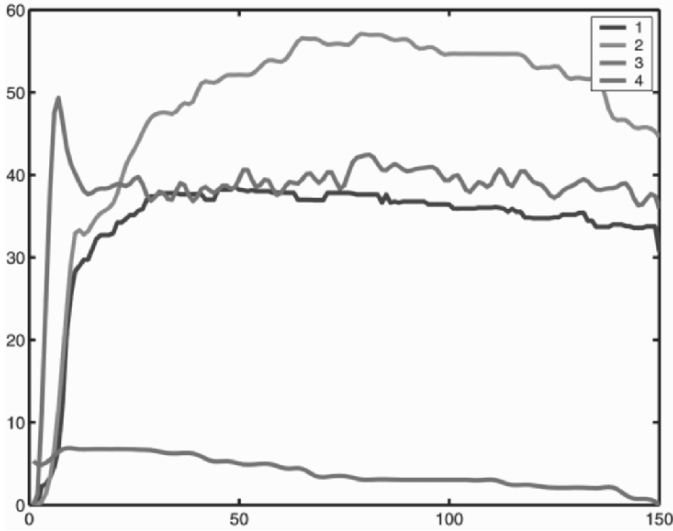
Figure 22. Cortex intensity vs. scan number from 4 subjects. There are 4 seconds between each scan. Subjects 1 and 2 have acute rejection, subject 3 is normal, and subject 4 is chronic glomerulopathy proved by biopsy. In these cortical renograms the normal patient shows the expected abrupt increase in intensity along with a fast decrease, followed by a constant valley and a slow decrease. On the other hand, these abrupt patterns are not seen in acute rejection patients; there is no definite peak, and the time to reach peak intensity is delayed. Subject 4 shows that DCE-MRI is also powerful in distinguishing other diseases. See attached CD for color version.

9. CONCLUSION

In this chapter we presented a framework for the detection of acute renal rejection from Dynamic Contrast Enhanced Magnetic Resonance Images that includes segmentation of kidneys from abdomen images, nonrigid registration, and Bayes classification. For segmentation of kidneys from the abdomen images, we introduced a new deformable model that evolves with both the gray-level information of a given abdomen image, and the shape information obtained from a database of manually segmented kidneys. The energy function of this deformable model is a combination of (i) the gray-level density and (ii) the prior shape information as a 1D density function. For these density estimations we introduced a modified EM algorithm that closely approximates the densities. Following segmentation, we introduced a nonrigid registration algorithm that deforms the kidney object on isocontours instead of a square lattice, which provides more degrees of freedom to obtain accurate deformation. After nonrigid registration, the kidney is segmented into cortex and medulla, and the average gray-level value of the cortex for the whole sequence of a patient is plotted. The features extracted from these signal

plots (renograms) undergo Bayesian classification to understand if the transplanted kidney is undergoing acute rejection or if it is functioning normally.

Our future work will include testing more patients, and testing the robustness of our approach. In addition, we will try to classify other possible diseases that occur after transplantation, and even try to understand the severity of rejection. With such developments we believe that analysis of DCE-MRI imagery has a high potential for replacing the current nuclear imaging tests or invasive biopsy techniques.

10. REFERENCES

1. *2000 annual report of the U.S. scientific registry of transplant recipients and the organ procure-ment and transplantation network: transplant data 1990–1999*. 2001. Richmond, VA: United Network for Organ Sharing, Richmond, VA.

2. Sharma RK, Gupta RK, Poptani H, Pandey CM, Gujral RB, Bhandari M. 1995. The magnetic resonance renogram in renal transplant evaluation using dynamic contrast-enhanced MR imaging. *Radiology* **59**:1405–1409.

3. Kasiske BL, Keane WF. 1996. Laboratory assessment of renal disease: clearance, urinalysis, and renal biopsy. In *The kidney*, 5th ed., pp. 1137–1173. Ed BM Brenner, FC Rector. Philadelphia: Saunders.

4. Bennett HF, Li D. 1997. MR imaging of renal function. *Magn Reson Imaging Clin North Am* **5**(1):107–126.

5. Giele ELW. 2002. *Computer methods for semi-automatic MR renogram determination*. PhD dissertation. Department of Electrical Engineering, University of Technology, Eindhoven.

6. Taylor A, Nally JV. 1995. Clinical applications of renal scintigraphy. *Am J Roentgenol* **164**:31–41.

7. Katzberg RW, Buonocore MH, Ivanovic M, Pellot-Barakat C, Ryan RM, Whang K, Brock JM, Jones CD. 2001. Functional, dynamic and anatomic MR urography: feasibility and preliminary findings. *Acad Radiol* **8**:1083–1099.

8. Tublin ME, Bude RO, Platt JF. 2003. The resistive index in renal Doppler sonography: where do we stand? *Am J Roentgenol* **180**(4):885–892.

9. Huang J, Chow L, Sommer FG, Li KCP. 2001. Power Doppler imaging and resistance index measurement in the evaluation of acute renal transplant rejection. *J Clin Ultrasound* **29**:483–490.

10. Turetschek K, Nasel C, Wunderbaldinger P, Diem K, Hittmair K, Mostbeck GH. 1996. Power Doppler versus color Doppler imaging in renal allograft evaluation. *J Ultrasound Med* **15**(7):517–522.

11. Trillaud H, Merville P, Tran Le Linh P, Palussiere J, Potaux L, Grenier N. 1998. Color Doppler sonography in early renal transplantation follow-up: resistive index measurements versus power Doppler sonography. *Am J Roentgenol* **171**(6):1611–16115.

12. Yang D, Ye Q, Williams M, Sun Y, Hu TCC, Williams DS, Moura JMF, Ho C. 2001. USPIO enhanced dynamic MRI: evaluation of normal and transplanted rat kidneys. *Magn Reson Med* **46**:1152–1163.

13. Chan L. 1999. Transplant rejection and its treatment. In *Atlas of diseases of the kidney*, Vol. 5, chap. 9. Series Ed RW Schrier. Philadelphia: Current Medicine Inc.

14. Szolar DH, Preidler K, Ebner F, Kammerhuber F, Horn S, Ratschek M, Ranner G, Petritsch P, Horina JH. 1997. Functional magnetic resonance imaging of the human renal allografts during the post-transplant period: preliminary observations. *Magn Reson Imaging* **15**(7):727–735.

15. Lorraine KS, Racusen C. 1999. Acute tubular necrosis in an allograft. *Atlas of diseases of the kidney*, Vol. 1, chap. 10. Series Ed RW Schrier. Philadelphia: Current Medicine Inc.

16. Krestin GP, Friedmann G, Steinbrich W. 1988. Gd-DTPA enhanced fast dynamic MRI of the kidneys and adrenals. *Diagn Imaging Int* **4**:40–44.

17. Krestin GP, Friedmann G, Steinbrich W. 1988. Quantitative evaluation of renal function with rapid dynamic gadolinium-DTPA enhanced MRI. In *Proceedings of the international society for magnetic resonance in medicine*, Book of Abstracts. Los Angeles: MRSTS.

18. Frank JA, Choyke PL, Girton M. 1989. Gadolinium-DTPA enhanced dynamic MR imaging in the evaluation of cisplatinum nephrotoxicity. *J Comput Assist Tomogr* **13**:448–459.

19. Knesplova L, Krestin GP. 1998. Magnetic resonance in the assessment of renal function. *Eur Radiol* **8**:201–211.

20. Choyke PL, Frank JA, Girton ME, Inscoe SW, Carvlin MJ, Black JL, Austin HA, Dwyer AJ. 1989. Dynamic Gd–DTPA-enhanced MR imaging of the kidney: experimental results. *Radiology* **170**:713–720.

21. Sun Y, Jolly M, Moura JMF. 2004. Integrated registration of dynamic renal perfusion MR images. In *Proceedings of the IEEE international conference on image processing*, pp. 1923–1926. Washington, DC: IEEE

22. Yim PJ, Marcos HB, McAuliffe M, McGarry D, Heaton I, Choyke PL. 2001. Registration of time-series contrast enhanced magnetic resonance images for renography. In *Proceedings of the 14th IEEE symposium on computer-based medical systems*, pp. 516–520. Washington, DC: IEEE.

23. Sun Y, Moura JMF, Ho C. 2004. Subpixel registration in renal perfusion MR image sequence. In *Proceedings of an IEEE international symposium on biomedical imaging*, pp. 700–703, Washington, DC: IEEE.

24. Sun Y, Moura JMF, Yang D, Ye Q, Ho C. 2002. Kidney segmentation in MRI sequences using temporal dynamics. In *Proceedings of an IEEE international symposium on biomedical imaging*, pp. 98–101. Washington, DC: IEEE.

25. Gerig G, Kikinis R, Kuoni W, van Schulthess GK, Kubler O. 1992. Semiautomated ROI analysis in dynamic MRI studies, part I: image analysis tools for automatic correction of organ displacements. *IEEE Trans Image Process* **11**:(2):221–232.

26. von Schulthess GK, Kuoni W, Gerig G, Duewell S, Krestin G. 1991. Semiautomated ROI analysis in dynamic MRI studies, part II: application to renal function examination, first experiences. *J Comput Assist Tomogr* **2**:733–741.

27. Liang Z, Lauterbur PC. 1994. An efficient method for dynamic magnetic resonance imaging. *IEEE Trans Med Imaging* **13**(4):677–686.

28. Giele ELW, de Priester JA, Blom JA, den Boer JA, van Engelshoven JMA, Hasman A, Geerlings M. 2001. Movement correction of the kidney in dynamic MRI scans using FFT phase difference movement detection. *J Magn Reson Imaging* **14**(6):741–749.

29. Vosshenrich R, Kallerhoff M, Grone HJ, Fischer U, Funke M, Kopka L, Siebert G, Ringert RH, Grabbe E. 1996. Detection of renal ischemic lesions using Gd-DTPA enhanced turbo flash MRI: experimental and clinical results. *J Comput Assist Tomogr* **20**(2):236–243.

30. Munechika H, Sullivan DC, Hedlund LW, Beam CA, Sostman HD, Herfkens RJ, Pelc NJ. 1991. Evaluation of acute renal failure with magnetic resonance imaging using gradient-echo and Gd-DTPA. *Invest Radiol* **26**(1):22–27.

31. Carvlin MJ, Arger PH, Kundel HL, Axel L, Dougherty L, Kassab EA, Moore B. 1987. Acute tubular necrosis: use of gadolinium-DTPA and fast MR imaging to evaluate renal function in the rabbit. *J Comput Assist Tomogr* **11**(3):488–95.

32. Dalla-Palma L, Panzetta G, Pozzi-Mucelli RS, Galli G, Cova M, Meduri S. 2000. Dynamic magnetic resonance imaging in the assessment of chronic medical nephropathies with impaired renal function. *Eur Radiol* **10**(2):280–286.

33. Kikinis R, von Schulthess GK, Jager P, Durr R, Bino M, Kuoni W, Kubler O. 1987. Normal and hydronephrotic kidney: evaluation of renal function with contrast-enhanced MR imaging. *Radiology* **165**(3):837–842.

34. Semelka RC, Hricak H, Tomei E, Floth A, Stoller M. 1990. Obstructive nephropathy: evaluation with dynamic Gd-DTPA-enhanced MR imaging. *Radiology* **175**:797–803.

35. Beckmann N, Joergensen J, Bruttel K, Rudin M, Schuurman HJ. 1996. Magnetic resonance imaging for the evaluation of rejection of a kidney allograft in the rat. *Transpl Int* 9(3):175–83.

36. Preidler KW, Szolar D, Schreyer H, Ebner F, Kern R, Holzer H, Horina JH. 1996. Differentiation of delayed kidney graft function with gadolinium-DTPA-enhanced magnetic resonance imaging and Doppler ultrasound. *Invest Radiol* 31(6):364–371.

37. El-Diasty T, Mansour O, Farouk A. 2003. Diuretic contrast enhanced mru versus ivu for depiction of non-dilated urinary tract. *Abd Imaging* 28:135–145.

38. Laurent D, Poirier K, Wasvary J, Rudin M. 2002. Effect of essential hypertension on kidney function as measured in rat by dynamic MRI. *Magn Reson Med* 47(1):127–131.

39. Krestin GP. 1994. Magnetic resonance imaging of the kidneys: current status. *Magn Reson Q* 10:2–21.

40. Sun Y. 2004. *Registration and segmentation in perfusion MRI: kidneys and hearts*. PhD dissertation, Department of Electrical and Computer Engineering, Carnegie Mellon University, Pittsburg.

41. de Priester JA, Kessels AG, Giele EL, den Boer JA, Christiaans MHL, Hasman A, van Engelshoven JMA. 2001. MR renography by semiautomated image analysis: performance in renal transplant recipients. *J Magn Reson Imaging* 14(2):134–140.

42. Boykov Y, Lee VS, Rusinek H, Bansal R. 2001. Segmentation of dynamic N–D data sets via graph cuts using Markov models. In *Proceedings of the 4th international conference on medical image computing and computer-assisted intervention (MICCAI)*. Lecture Notes in Computer Science, Vol. 2208, pp. 1058–1066. Utrecht: Springer.

43. Sun Y, Yang D, Ye Q, Williams M, Moura JMF, Boada F, Liang Z, Ho C. 2003. Improving spatiotemporal resolution of USPIO-enhanced dynamic imaging of rat kidneys. *Magn Reson Imaging* 21:593–598.

44. Chan TF, Vese LA. 2001. Active contours without edges. *IEEE Trans Image Process* 10(2):266–277.

45. Ibanez L, Schroeder W, Ng L, Cates J, and the Insight Software Consortium. 2005. *The ITK software guide*. Clifton Park, NY: Kitware Inc.

46. Sethian JA. 1996. *Level set methods and fast marching methods*. Cambridge: Cambridge UP.

47. Caselles V, Kimmel R, Sapiro G. 1997. Geodesic active contours. *Int J Comput Vision* 22(1):61–79.

48. Rousson M, Paragios N. 2002. Shape priors for level set representations. In *Proceedings of the 7th European conference on computer vision, part II (ECCV'02)*. Lecture Notes in Computer Science, Vol. 2751, pp. 78–92. Berlin: Springer.

49. Leventon M, Grimson WL, Faugeras O. 2000. Statistical shape influence in geodesic active contours. In *Proceedings of the IEEE conference on computer vision and pattern recognition*, pp. 1316–1324. Washington, DC: IEEE Computer Society.

50. Chen Y, Thiruvenkadam S, Tagare H, Huang F, Wilson D. 2001. On the incorporation of shape priors into geometric active contours. In *IEEE workshop on variational and level set methods*, pp. 145–152, Washington, DC: IEEE.

51. Tsai A, Yezzi AJ, Wells WM, Tempany C, Tucker D, Fan A, Eric W, Grimson L, Willsky AS. 2001. Model-based curve evolution technique for image segmentation. In *Proceedings of the IEEE conference on computer vision and pattern recognition*, pp. 463–468, Washington, DC: IEEE Computer Society.

52. Paragios N. 2003. A level set approach for shape-driven segmentation and tracking of the left ventricle. *IEEE Trans Med Imaging* 22:773–776.

53. Litvin A, Karl WC. 2003. Level set-based segmentation using data driven shape prior on feature histograms. In *IEEE workshop on statistical signal processing*, pp. 166–169. Washington, DC: IEEE.

54. Tsai A, Wells W, Warfield SK, Willsky AS. 2004. Level set methods in an em framework for shape classification and estimation. In *Proceedings of the international conference on medical image computing and computer-assisted intervention (MICCAI)*. Lecture Notes in Computer Science, Vol. 2211, pp. 1–9. Utrecht: Springer.

55. Yang J, Duncan J. 2004. 3d image segmentation of deformable objects with joint shape-intensity prior models using level sets. *Med Image Anal* **8**:285–294.
56. Yuksel SE, El-Baz A, Shi H, Farag AA, El-Ghar MEA, Eldiasty TA, Ghoneim MA. 2005. Automatic detection of renal rejection after kidney transplantation. In *Proceedings of the conference on computer assisted radiology and surgery (CARS)*, pp. 773–778. Berlin: Springer.
57. Witkin A, Kass M, Terzopoulos D. 1987. Snakes: Active contour models. *Int J Comput Vision* **1**:321–331.
58. El-Baz A, Yuksel SE, Shi H, Farag AA, El-Ghar MA, Eldiasty T, Ghoneim MA. 2005. 2d and 3d shape-based segmentation using deformable models. In *Proceedings of the international conference on medical image computing and computer-assisted intervention (MICCAI)*. Lecture Notes in Computer Science, Vol. 2212,pp. 821–829. Utrecht: Springer.
59. Viola P, Wells WM. 1995. Alignment by maximization of mutual information. In *Proceedings of the 5th international conference on computer vision*, pp. 16–23. Washington, DC: IEEE Computer Society.
60. Tsai A, Yezzi A, Wells W, Tempany C, Tucker D, Fan A, Grimson E, Willsky A. 2003. A shape-based approach to curve evolution for segmentation of medical imagery. *IEEE Trans Med Imaging* **22**(2):137–154.
61. Webb A. 2002. *Statistical pattern recognition*. 2nd. ed. Chichester: J. Wiley & Sons.
62. Schlesinger MI. 1968. A connection between supervised and unsupervised learning in pattern recognition. *Kibernetika* **2**:81–88.
63. Lamperti JW. 1996. *Probability*. New York: J. Wiley & Sons.
64. te Strake L, Kool LJS, Paul LC, Tegzess AM, Weening JJ, Hermans J, Doornbos J, Bluemm RG, Bloem JL. 1988. Magnetic resonance imaging of renal transplants: its value in the differentiation of acute rejection and cyclosporin A nephrotoxicity. *Clin Radiol* **39**(3):220–228.
65. Farag, AA, El-Baz A, Gimel'farb G. 2004. Density estimation using modified expectation-maximization for a linear combination of gaussians. In *Proceding of the IEEE international conference on image processing*, Vol. 3, pp. 1871–1874. Washington, DC: IEEE Computer Society.